Probabilistic estimates of California climate change by the 2060s using statistical and dynamical downscaling

David W. Pierce[1], Tapash Das[1], Daniel R. Cayan[1], Edwin P. Maurer[2], Norman Miller[3],

Yan Bao[3], M. Kanamitsu[1], Kei Yoshimura[1], Mark A. Snyder[4], Lisa C. Sloan[4], Guido Franco[5],

Mary Tyree[1]

[1]Division of Climate, Atmospheric Sciences, and Physical Oceanography, Scripps
Institution of Oceanography, La Jolla, CA

[2]Civil Engineering Department, Santa Clara University, Santa Clara, CA

[3]Earth Sciences Division, University of California, Berkeley, Berkeley, CA

[4]Climate Change and Impacts Laboratory, Department of Earth Sciences, University of
California, Santa Cruz, Santa Cruz, CA

[5]California Energy Commission, Sacramento, CA

Version 1.0

21 March 2011

Abstract

Sixteen global general circulation models were used to develop probabilistic projections of temperature (T) and precipitation (P) change over California by the 2060s. The global models were downscaled with two statistical techniques and three nested dynamical regional climate models, although not all global models were downscaled with all techniques. The focus is on changes in daily distributions of T and P, which are important for a range of applications in energy use, water management, and agriculture. Similar to previous studies, the T climate change signal is more consistent geographically and across models than the P signal. The T changes also tend to agree more across downscaling techniques than the P changes. Year-to-year natural internal climate variability is roughly of similar magnitude to the projected T changes, but natural variability is an order of magnitude larger than the projected P changes. The distribution of warmest days in July tends to increase uniformly, except along the North coast of the state, where the warmest days show less warming. In the monthly average, July temperatures shift enough that that the hottest July found in any simulation over the historical period becomes a modestly cool July in the future period. The distribution of warmest days in January is little changed at the median or below, but becomes notably warmer on the few warmest days of the year. As a result, Januarys as cold as any found in the historical period are still found in the 2060s, but the median and maximum monthly average temperatures increase notably. Although the annual P changes are small compared to interannual or intermodel variability, the annual change is composed of seasonally varying changes in storm intensity and number of stormy days that are themselves much larger, but tend to cancel in the annual mean. Winters show modest wetter conditions in the North of the state due to a strong increase in storm intensity coupled with a weak decrease in the number of stormy days, while spring and autumn show drying due to a strong decrease in the number of stormy days coupled with a weak increase in storm intensity. The dynamical downscaling techniques project increasing precipitation in the Southeastern part of the state, which is influenced by the North American monsoon, due to an increase in both the number of precipitating days and the average P on those days.

1. Introduction

California has a confluence of factors that make it particularly vulnerable to anthropogenically-induced climate change (e.g., Wilkinson et al. 2002, Hayhoe et al. 2004, Cayan et al. 2006, Dettinger and Culberson 2008). The long coastline is subject to sea level rise, which will affect erosion and saltwater intrusion into estuaries such as the sensitive Sacramento-San Joaquin river delta. Warming and precipitation changes will directly impact crops and pests in the agricultural and wine-producing regions, and affect regional water resources and flood risk through changes in the snow line, snowpack, and evapotranspiration. The California state government recognizes these potential vulnerabilities, and is encouraging the use of climate projections in long-term planning so impacts can be minimized. Indeed, anthropogenic effects can already be seen in the temperature and hydrology of the region (Barnett et al. 2008, Pierce et al. 2008, Bonfils et al. 2008, Hidalgo et al. 2009, Das et al. 2009; cf. Maurer et al. 2007, who examined a smaller region).

Regionalized climate change scenarios can provide the basis for this long-term planning. Beyond scenarios, however, the decision making community needs climate projections to be expressed probabilistically (e.g. Manning et al. 2009). This approach facilitates incorporating projections into risk-based planning, and provides a framework to identify strategies for adaptive resource management (e.g., Brekke et al., 2009). A probabilistic assessment is important partly because different global climate models produce different future climates given the same forcing, and partly because natural climate variability means even a set of identical Earths would form a distribution of future climates.

The primary purpose of this work is to present probabilistic projections of temperature (T) and precipitation (P) change over California by the 2060s. Hydrological variables such as snowpack, runoff, and flooding are addressed using a surface hydrological model, and will be presented in a separate work. The ultimate basis for the projections are global climate model (GCM) simulations from the Coupled Model Intercomparison Project, version 3 (CMIP3; Meehl et al., 2007). Since the GCMs are not

independent (sometimes sharing, for example, convection or microphysics parameterizations), and do not uniformly sample model uncertainties, the distributions shown here are not true estimates of the probability of future climate changes. Instead, they present best-guess estimates of future climate change given our current ability to understand and model climate as reflected in the CMIP3 archive.

Uncertainty in climate projections arises from three sources (Hawkins and Sutton 2009): unknown future emissions, climate model deficiencies, and natural climate variability. The present study includes the latter two sources evaluated in a probabilistic framework. The projections may change in the future as our understanding increases, but many practical applications of climate information have long decision lead times that could use climate change information now (Anderson et al, 2008). This work is aimed at developing a framework and providing current, state of the science climate change estimates for those longer-term strategic and planning needs.

Current GCMs do not resolve such topographic features as the Sierra Nevada or California coastal range, which affect regional and local climate. Therefore, we downscale the global models to a ~12 km grid using three regional dynamic models and two statistical methods. We used both statistical and dynamical techniques because each has different strengths and limitations. The secondary purpose of this work is to compare the climate projections from the dynamical and statistical downscaling techniques and address how they systematically differ.

Natural internal climate variability in California is strongly influenced by the El Nino/Southern Oscillation (ENSO) and Pacific Decadal Oscillation (PDO) (Cayan, 1996). Although ENSO's time scale of roughly 2-7 years means that its effects will begin to average out over the decadal time scale considered here, there could be a net effect if the frequency of ENSO events changes. There is currently no consensus on whether this will happen (Yeh et al. 2009, Collins et al. 2010), and while GCM simulations of ENSO have gotten better over the years, they still have notable flaws (AchutaRao and Sperber, 2006). The spectrum of the PDO is nearly red (e.g., Pierce 2001), so the longer the timescale of interest, the more power the PDO has at that timescale. As a result, prolonged periods of positive or

4

negative PDO can (and likely will) add to the anthropogenic climate signal to give the overall climate in California's future. There is also some evidence that anthropogenic forcing could influence the state of the PDO (Meehl et al., 2009). We include effects of natural internal climate variability in our analysis.

There is a substantial body of literature examining the present, and usually future, climate of the western U.S. with some combination of single or multiple GCMs and statistical or dynamical downscaling (e.g., Dickinson et al. 1989, Giorgi et al. 1994, Leung and Ghan, 1999a, 1999b; Takle et al., 1999; Pan et al, 2001; Kim, 2001 and 2005; Hayhoe et al., 2004; Brekke et al. 2004; Coquard et al. 2004; Leung et al. 2004; Brekke et al. 2004; Maurer and Duffy 2005; Snyder and Sloan 2005; Duffy et al. 2006; Maurer 2007; Vicuna et al. 2007; Liang et al. 2008; Chin et al. 2010). Some common themes emerge from these efforts. First, different GCMs produce different magnitudes of warming and a range of precipitation changes. Second, regional climate models (RCMs) introduce another source of variation, with different regional models yielding different outcomes for the same driving GCM. Third, projected temperature changes over California are consistently positive, but precipitation changes can vary in sign across models. Fourth, even with the divergent precipitation projections, the effect on California's hydrology is substantial; snowpack declines and runoff shifts to earlier in the water year, with elevation-dependent effects due to the colder temperatures at higher elevations. And fifth, when simulating historical climate structure, most if not all model simulations exhibit biases, which are assumed to also affect the projected climate as well.

Given this body of previous work in the California region, it is perhaps surprising that major gaps remain. Few of the studies approached the problem probabilistically, which is useful for planning purposes. Also, almost all the studies referenced above deal exclusively with monthly data. Only Leung et al. 2004, Hayhoe et al. 2004, and Kim 2005 analyze the future daily data. Daily information is needed in a wide variety of applications, such as energy use (where sequences of three or more days of hot temperatures result in high air conditioner loads), agriculture (where daily minimum and maximum temperatures can affect crops and pests), and water management (where a few days of intense

precipitation can generate floods). Finally, although some of the studies referenced above use dynamical downscaling and some use statistical, none used both and compared the two (cf. Hay and Clark 2003, who used both, but over the historical period only and examined runoff rather than T and P). With the availability of a downloadable archive of statistically downscaled data for the western U.S. (http://gdo-dcp.ucllnl.org/downscaled_cmip3_projections/dcpInterface.html), it is worth characterizing how statistical and dynamical downscaled results differ in this region. Similar issues have been addressed in other regions; for example, Europe in the PRUDENCE (Christensen et al., 2007) and ENSEMBLES (Kjellstrom and Giorgi, 2010) projects, and the UK with the Climate Projections project (http://ukclimateprojections.defra.gov.uk/).

2. Data and Methods

The work shown here builds on Miller et al. (2009), who examined the ability of the dynamic regional climate models (RCMs) used here to simulate California's historical climate when driven with boundary conditions from the NCEP reanalysis II (Kanamitsu et al. 2002). Details of the RCMs are given in that work, as well as a comparison of the RCMs' climatology to observations. However, users of the projections should understand that the RCMs perform better when driven by historical (reanalysis) conditions than when driven by boundary conditions from coupled climate models that have their own biases and errors. This is one of the motivations for bias correcting the RCM output, as explained below.

Our model runs can be organized by the downscaling method used: dynamical, statistical via bias correction with spatial disaggregation (BCSD), or statistical via bias correction with constructed analogues (BCCA). All approaches downscale to an approximately a $1/8^O$ x $1/8^O$ (~ 12 km) spatial resolution. Table 1 lists the various models used for each downscaling technique, and further details are given in the next subsections. Not all GCMs were downscaled with all three techniques. This is partly because of the computer time required for the dynamical downscaling, and partly because the daily data required for dynamical and BCCA downscaling was only available for a few GCMs.

6

The steep computational resources required for the dynamical downscaling imposed constraints on this work. First, only limited time periods were covered in the RCM runs: 1985-94 (the "historical period") and 2060-2069 (the "future period"). Although the statistical downscaling covered 1950-2099, for consistency we concentrate on the 1985-1994 and 2060-2069 periods for all downscaling techniques and models. Second, only global models driven by the SRES A2 emissions scenario were dynamically downscaled. The strategic choice was made to prefer more model runs using one emissions scenario over fewer runs with multiple emissions scenarios. We note that the 2060s is about the last decade where globally averaged surface temperatures from the A2, B1, and A1B emissions scenarios do not show a clear separation (IPCC 2007, Fig. SPM.5).

The 10-year spans are too short to examine natural climate variability from ENSO and the PDO in any one model run. However, we partially make up for this by using 4 to 16 models at a time (depending on the downscaling technique). Natural variability is not synchronized across the models, so this samples different phases of the ENSO and PDO, which means our trend estimates averaged across models will be more robust to natural variability. However we cannot unambiguously determine whether 10-yr mean differences between models are due to sampling different phases of the PDO or inter-model spread in the mean climate projection. When we estimate the variability arising from natural causes versus model spread, the sum of these two effects is correct but the split will be biased towards weighting model spread more. I.e., some difference between runs that arises from sampling different phases of the PDO on a 10-yr timescale will be ascribed to model spread.

Results are presented as averages over the 11 California climate regions identified by Abatzoglou et al. 2009. As shown there, these regions do a better job representing California's diverse mix of climate regimes than the standard U.S. climate divisions.

2.1 Dynamical downscaling

Three different dynamical RCMs are used for downscaling the GCM data: the weather research forecast model (WRF), the regional spectral model (RSM), and the regional climate model, version 3 (RegCM3). The models will only be described briefly here; details are given in the references.

a) Regional Climate Model version 3 (RegCM3)

RegCM3 is a third-generation regional-scale climate model derived from the National Center for Atmospheric Research-Pennsylvania State (NCAR-PSU) MM5 mesoscale model (Pal et al. 2007). RegCM3 has the same dynamical core as MM5, the CCM3 radiative transfer package, and the Biosphere-Atmosphere Transfer Scheme (BATS) land surface model (Dickinson et al., 1986; Giorgi et al., 2003). RegCM has been validated against observations of modern-day climate in multiple domains, and does well in simulating the spatial and temporal climate features of California (Snyder et al., 2002, Bell et al., 2004). For this study RegCM3 was configured with the Holtslag boundary layer scheme (Holtslag et al., 1990), Grell cumulus scheme (Grell, 1993) with the Fritsch and Chappell closure scheme (Fritsch and Chappell, 1980), and the Zeng (1998) ocean flux parameterization. The model domain is centered over California with a horizontal resolution of 10 km and 18 levels in the vertical.

b) Weather Research and Forecasting model (WRF)

We use a version of NCAR WRF version 3 coupled to the community land surface model version 3.5 (CLM3.5; Oleson et al. 2004), referred to as "WRF-CLM3" in Miller et al. 2009. The combination has an advanced land surface scheme with sub-grid representation for snow and vegetation, lateral hydrologic flow capability, and the potential for time-evolving plant functional types. The WRF model is set up with the Kain-Fritsch convection parameterization for cumulus clouds (Kain and Fritsch 1993), the Yonsei University (YSU) planetary boundary layer (PBL) scheme (Hong and Pan 1996), and the Medium Range Forecast Model turbulence closure scheme (Mellor and Yamada 1982). The microphysics package

used here is the WRF Single-Moment 3-class (WSM3) scheme (Hong et al. 2004), and the Rapid

Radiative Transfer Model (RRTM) based on Mlawer et al. (1997) is used for describing longwave

radiation transfer within the atmosphere and to the surface, and the shortwave scheme developed by

Dudhia (1989).

c) Regional Spectral Model (RSM)

The version of the regional spectral model (RSM) used here is a development of the National

Centers for Environmental Prediction (NCEP) global spectral model (GSM). The original regional code

has been modified to have greater flexibility and increased efficiency (Kanamitsu et al., 2005). The RSM

uses a two-dimensional spectral decomposition, and is implemented with so-called "spectral nudging",

i.e., relaxation towards the low-frequency components of the global simulation over the regional domain

(Kanamaru and Kanamitsu 2007). The configuration used here is similar to that used to generate the 10-

km California Reanalysis Downscaling (CaRD10) data set (Kanamitsu and Kanamuru, 2007). A scale-

selective bias correction (SSBC) was used during these runs (Kanamaru and Kanamitsu 2007). The Noah

land surface model with four soil layers was used, and cloud water and cloudiness are implemented as

prognostic variables (Tiedtke 1993; Iacobellis and Sommerville 2000).

2.2 Statistical downscaling

We use two different statistical downscaling techniques. Both operate on bias-corrected GCM

data; the bias correction (BC) procedure is described in section 2.3.

a) Bias Correction with Spatial Disaggregation (BCSD)

BCSD (Wood et al. 2002, 2004) generates daily, fine-resolution ($1/8^o$ x $1/8^o$ in this

implementation) fields from monthly, bias-corrected GCM data by randomly selecting an analogue month

from the historical observations such that the selected month is the same month of the year as the data

being downscaled. Monthly GCM anomalies are interpolated onto the fine-scale grid, then applied, by

9

offsetting (for temperature) or scaling (for precipitation), to the long term mean at the fine scale. This produces a fine scale monthly downscaled value. The daily observed data for the analogue month on the fine-scale grid is then offset (for temperature) or scaled (for precipitation) so that each grid cell's monthly mean matches the monthly downscaled value. Since analogue months from the historical period are used to generate the daily sequences, we do not analyze BCSD-generated distributions of daily future climate variables. BCSD downscaling is used, for example, by Hayhoe et al. (2004), Maurer (2007), and Vicuna et al. (2007).

b) Bias Correction with Constructed Analogues (BCCA)

BCCA uses bias correction along with downscaling of daily GCM fields via constructed analogues (Hidalgo et al., 2008; Maurer et al. 2010). BCCA is therefore the CANA method described by Miller et al. (2009) along with a BC step applied to the GCM temperature and precipitation fields. The constructed analogue technique starts with a library of daily historical observations on a $1/8^o$ x $1/8^o$ grid. This fine scale data is coarsened to the GCM grid, and the 30 best matches between the GCM fields for that day and the coarsened observations are computed. The 30 weights obtained from the matching process are then applied to the fine scale data.

2.3 Bias correction

All T and P fields, whether downscaled statistically or dynamically, underwent a bias correction procedure. This is necessary because the project's focus was on hydrological and other applications, and even current state-of-the-art GCMs/RCMs generate T and P fields with biases, often due to biases in the original global fields (e.g., Wood et al. 2004, Duffy et al. 2006, Liang et al. 2008). The output of the GCMs was bias corrected before statistical downscaling, while the output of the dynamical RCMs was bias corrected after being generated. Although similar, the BC procedures for the three data sets (BCSD, BCCA, and the RCMs) differ in important details.

BCSD starts with monthly GCM data, which we bias correct using the quantile-mapping technique described in Maurer (2007), based on Wood et al. (2002, 2004). The mapping parameters are determined for each month over 1950-99, then applied to the future period. The assumption is that the biases are unchanged in the future (cf. Liang et al. 2008). As noted by Wood et al. (2004), a full 50 year period is preferable when bias-correcting monthly GCM output. For temperature, the linear trend from the GCM output (interpolated to the fine scale grid) was removed at each point before the BC procedure was applied, and then added back in afterwards. The reason for this is explained by Wood et al. (2004): as temperatures rise in the future they are found more frequently outside the historic range, requiring excessive extrapolation during the quantile mapping. Precipitation, with typically much greater interannual variability than temperature, does not generally experience trends that exhibit this problem during remapping, so the trend removal and replacement was not applied. This procedure has the advantage that the final result preserves the original trend in the global model, but the disadvantage that the resulting trend is essentially that of the interpolated global model.

The BCCA and RCM data are daily. We bias correct the daily data using a similar quantile mapping technique, described in Maurer et al. (2010). The historical period used for the monthly BCCA downscaling was the 50 year span 1950-1999, but only the 10-yr period 1984-1995 is available for the RCM data. New results suggest that when bias correcting daily (instead of monthly) data, 10 years is adequate (Maurer et al., manuscript in preparation).

In contrast to BCSD, the global trend was not removed and then reapplied for the BCCA and RCM data, since the motivation for trend removal and replacement described above is not as strong for daily data. For example, since a large portion of the trend in daily temperatures is due to more frequent warm temperatures (as opposed to relatively few record hot temperatures) (Dettinger et al., 2004), which are represented in the historic period, the trend removal and replacement procedure is less necessary. This also means that the trend in these data sets is free to differ from the GCM trend. Since the basic

11

assumption of downscaling is that it adds regionalized information to the global signal, this is a desirable characteristic.

However, the bias correction itself can modify the global trend. Table 2 illustrates this for July average daily temperature at one grid point. Bias correction modifies the variance of the GCM output, since GCM simulations inevitably contain biases in variance, skew, and higher moments. The historical mapping is applied to future projections, so this process changes the statistical properties of the GCM projections. This table shows that when bias correction increases the standard deviation of the monthly data, then the low-frequency trend increases as well; when BC decreases the standard deviation, the trend decreases. In essence, the procedure assumes that errors in the amplitude of variability apply equally on all timescales, from daily to the secular trend.

Statistical downscaling methods that remove the large-scale trend prior to bias correction and then add it back in (BCSD in this study) will thus preserve the GCM-simulated trend, while BCCA (as used here) will be affected by the trend modification shown in Table 2. This can be seen in BCCA's downscaled output (Figure 2). Whether the trend modification is appropriate given GCM errors in simulating variability or if the raw simulated trend should be preserved through the downscaling procedure is currently an open question that is beyond the scope of this work.

3. Results

The probabilistic framework requires that several model runs be included to provide a distribution of projected outcomes. How should data from multiple GCMs, RCMs, and statistical downscaling techniques be combined? Often all models are weighted equally, an approach that was used in the last IPCC assessment (IPCC, 2007). However, it has also been suggested that model quality should be considered, with better models contributing more to the result (e.g., Giorgi and Mearns 2002, 2003). This has led to a discussion of which approach is better (e.g., Pierce et al. 2009; Knutti et al. 2010; Kjellstrom and Giorgi 2010; Christensen et al. 2010). For our purposes, we note that 1) Pierce et al. (2009) looked

specifically at the western U.S., and concluded that weighting by model quality does not make a difference to climate projections until after the time period considered here (the 2060s); 2) Giorgi and Mearns (2002) advocate weighting, but the actual difference this makes in the western U.S. is minimal (their Figs. 4 and 5); 3) Brekke et al. (2008) found little sensitivity to projected regional precipitation and temperature changes over northern California when culling GCMs based on historic skill in simulating relevant climate features; 4) Christensen et al. (2010), although considering a different region (Europe), conclude that "we do not find compelling evidence" that weighting provides improved results, yet it "adds another level of uncertainty to the generation of ensemble-based climate projections." Accordingly, we weight the models equally, although we still explore systematic differences between downscaling techniques.

Temperature changes are addressed in section 3.1, precipitation changes in 3.2, and joint temperature/precipitation changes in 3.3.

3.1 Temperature changes

Figure 1 shows an example "spaghetti plot" of all the runs considered here. The left panel shows temperature projections for the Sacramento/Central Valley region from all the model runs in deg-C relative to the historical period (1985-1994), while the right panel shows the same for precipitation (mm/day). Because of the bias correction, the mean and spread of the distributions are roughly similar in the historical period. The runs are free to develop differences in the future period, however.

Figure 2 shows the temperature changes by the 2060s, averaged across all models and downscaling techniques. The yearly-averaged warming (Fig. 2a) is on the order of 2.4 C. The downscaled data shows that the coastal regions experience less warming, with a typical value of about 1.9 C. Presumably this is due to the ocean's moderating influence, particularly given the coastal upwelling of cool subsurface water along California's coast in the summer. Inland locations show more warming, with

typical values approaching 2.6 C, which may have the potential to suppress coastal warming further via enhanced sea breezes in some locations (Lebassi et al, 2009).

Figures 2b through 2e shows that the mean warming has a pronounced seasonal signature, with the most warming (~3 C) in the summer (June-July-August; Fig. 2d), and the least warming (< 2 C) in the winter (Dec-Jan-Feb; Fig. 2b). Since energy use in California is dominated by summer cooling loads rather than winter heating loads, this warming pattern suggests that peak energy use could increase faster than would be expected if only the yearly averaged temperature changes were taken into account.

Figure 3 shows how temperature percentiles in the historical era change in the future. For example, the blue cross in panel a for the Sacramento/Central valley shows that the 50th percentile temperature in the historical period (x axis) will become the 17th percentile value in the 2060s (y axis). Interestingly, the curves in Fig. 3a start at the origin, which means that the coldest January monthly average temperatures in the historical period will still be experienced in the future. Climate change evidently will not eliminate unusually cold winter months in California, even judging coldness by historical standards. (Relative to the evolving mean, the coldest months become much more dramatic in the future, which might have implications for changing crops to those adapted to hotter conditions). This behavior is not isolated to only one GCM or downscaling technique; of the 26 runs (Table 1), 12 have at least one January in the 2060s that is about as cold, or colder, than the coldest historical January in the same model. Despite the existence of these cold Januarys in the future, Fig. 3a shows that the median monthly January temperature in the future will be warmer than 8 or 9 out of 10 Januarys today, and the warmest Januarys in the future are completely off the historical distribution. For instance, in the Northern California coast (top left of Fig. 3a), the warmest January found in the historical distributions of any model is only the 80th percentile found in 2060s. In sum, the overall picture for January is of occasional (rare) months as cold as any today, but notably warmer median temperatures, and with the warmest months warmer than any yet experienced.

The behavior of the warmest and coldest months is somewhat different in July (Fig. 3b). The curves still start nearly at the origin, but inspection showed that such a cold July only existed in one of the 26 runs. On the other hand, the difference in the warmest months is profound. Over most of the state, the warmest monthly average July found in the historical distribution of any model is only a 15-40th percentile event in the future period. I.e., a July that is exceptionally hot by current historical standards will become modestly cool in comparison to the new mean.

The yearly warming simulated by the various downscaling techniques is shown in Fig. 4. Results are shown only for the GFDL 2.1 global model, which was downscaled with all the techniques. This isolates the effect of the downscaling method used, since the different downscaling techniques were applied to different sets of models (Table 1). Temperature changes from the global model simulation are shown in Fig. 4f for comparison. The downscaling techniques generate similar values, and capture the decrease in warming near the coast that is poorly resolved in the global field. The main outlier is BCCA (Fig. 4e), which has 10-25% less warming than the other downscaling methods or global model, for the reasons outlined in Section 2.3 and Table 2.

a) Distributions of seasonal temperature change

Our main objective is to describe climate change in a probabilistic fashion for use by long-term planners. The exceedence probability of each year's seasonally averaged temperature change in the future period is shown in Fig. 5. The data in this figure has been re-sampled using the method described in Dettinger (2005), which fleshes out the distributions using a principal component analysis-based re-sampling technique applied to the variability around the model-mean climate change signal. I.e., it is a Monte Carlo technique that gives smoother estimates of the distribution by resampling the noise.

Figure 5 shows a distribution consisting of one value per year over the period 2060-69, so each model run contributes 10 values. It is not each model's change averaged over the future period, in which event each model run would contribute one value. The values are presented this way to include the effects

of natural internal climate variability. Our experience has been that users interested climate data for impacts studies are not always aware of the important role of natural climate variability. For those aware of it, including natural variability in the distributions is useful; for those who are not, we believe that conveying the importance of natural variability is essential for a proper understanding of climate change. The amplitude of natural variability will be quantitatively compared to the mean model warming and spread across the models in Figure 6, below.

Panels in Fig. 5 are arranged roughly geographically by climate region. The distributions are similar for all the regions, although the projected warming increases towards the Northeast, particularly in summer. Over most of the domain, there is a 90% chance of experiencing a warming of at least 1 C, and a 10% chance the warming will reach 3-4 C (depending on the season). Although summer (JJA) warming is largest in most of the domain, across the southern regions the differences between the seasons lessens, and autumn (Sep-Oct-Nov, SON) warming matches the JJA warming.

b) Forced changes versus natural internal climate variability

The distributions in Fig. 5 have contributions from three sources: 1) the average warming across models; 2) the difference in warming between models; and 3) natural internal climate variability. It is useful to distinguish these components. For example, an expected climate shift that is large compared to the natural variability could well have different planning implications than one that is small compared to the natural variability. Each simulation's mean warming is estimated as the mean of the 10 yearly values in the future period minus the mean of the 10 values in the historical period. Each simulation's natural internal climate variability is estimated from the difference between the 10 yearly values in the future period and the mean of the 10 values in the future period. Only the future period is used for this estimate in case natural variability is affected by the anthropogenic forcing.

Figure 6 shows these three components across the 11 climate regions, using both yearly (Fig. 6a) and seasonal (Figs. 6b-e) averages. Considering first the yearly average (Fig. 6a), the mean model-

16

estimated warming by the 2060s (green bars) is larger than the 90% confidence interval of natural internal variability (blue bars) in all regions. In practice, this means that the warming will be easily noticeable in the yearly average. The red lines show the 90% confidence interval in estimated warming across the models. The model-to-model variability is small compared to the magnitude of the projected warming. Even if we knew that one of the models used here was perfect and the rest wrong, it would make little difference to the warming estimates.

The other seasons in Fig. 6 tend to show a larger contribution from natural variability, which is understandable since fewer days are being averaged. This is most pronounced in winter (DJF, Fig. 6b), where the typical scale of year-to-year natural fluctuations in seasonally-averaged temperature is roughly twice the expected shift in temperatures. The uncertainly across models (red line) is a larger fraction of the mean warming as well. These tendencies are minimized in summer (JJA, Fig. 6d), where the temperature shifts are as large compared to the natural internal climate variability as seen in the yearly average.

c) Changes in daily temperature

Although the figures shown so far demonstrate the yearly and seasonal temperature changes, the actual values of daily temperatures are of interest for applications such as agriculture, health and energy demand. The BCSD downscaling technique uses only monthly data from the models, generating daily data by selecting matching months from the historical record. Since this does not preserve the models' sequence of daily values, only data pooled across the BCCA and dynamical downscaling techniques (Table 1) have been used for daily analyses of temperature and precipitation.

Figure 7 shows the cumulative distribution function of daily maximum temperature in July for the historical period (blue) and future period (red). Values have been plotted with an error function transformation on the Y axis, so a Gaussian distribution would form a straight line. The slope of such a line is proportional to the variability, with steeper slopes indicating less variability. All regions show a

17

distinct shift to a higher likelihood of warmer daily maximum temperatures at all probability levels. The shift is smallest, however, at the warmest temperatures in the Northern and central coastal regions, perhaps because of the moderating influence of cool upwelling ocean temperatures that are typically seen in summer along California's coast. Similar curves for daily July minimum temperature display more Gaussian behavior (straighter lines) and lack the reduced warming along the coast (not shown).

By contrast, January daily minimum temperatures (Fig. 8) show more warming at the highest percentile values and little change below the median. In other words, the projected experience on the ground in January will not be an increase in every day's minimum temperature so much as the appearance of rare days with temperature several degrees warmer than experienced before. The Southern California coast and mountains show a tendency towards a decrease in the temperature of the very coldest days as well. This same tendency is found more widely in January daily maximum temperature (not shown). While the slopes of the lines in Fig. 7 (July) tend to be the same or slightly steeper in the future, indicating similar or slightly reduced daily variability, the slopes of the lines in Fig. 8 (Jan) tend to be flatter in the future, indicating greater daily variability in projected January daily minimum (and maximum, not shown) temperatures.

Three-day averages of maximum daily temperature in summer are of interest to the energy industry, because people are more likely to use air conditioning by the third hot day. Figure 9 shows the distribution of the warmest 3-day average temperature in the year. The shifts seen here are proportionally much greater than seen in Figs. 7 or 8. Also, in all the inland locations the divergence between the historical and future distribution becomes more pronounced at the warmest temperatures. In these locations the difference between the historical and future distributions is quite astonishing. For example, in the San Joaquin valley, a 3-day run of 40 C or warmer temperatures is only a 1-in-100 occurrence in the historical simulations, but is a 1-in-2 occurrence in the future simulations. Or, the simulated 3-day average warmest temperature in the Anza-Borrego region is 46 C in the historical era, but 51 C in the future era. Increases along the coast are a less-alarming ~2 C, although even there the incidence of 3-day

18

maximum temperatures with a probability of < 0.01 in the historical era increases by a factor of 10. When comparing to the changes in maximum 1-day average temperature in the year (not shown), the increases in 3-day temperature are modestly larger at the high end of the distribution in the Northern and Central Coastal regions, but otherwise similar to Fig. 9.

3.2 Precipitation changes

Figure 10 shows the mean precipitation change (%) by the 2060s, averaged across all models and downscaling techniques. The overall tendency is for a small amount of drying in the southern part of the state (< 10%), and negligible changes in precipitation in the North. The patterns by season are more pronounced, with the northern part of the state experiencing wetter conditions in winter (Fig. 10b) that are nearly offset by drier conditions in the rest of the year (Figs. 10c through 10e). The southern part of the state shows moderate fractional drying in fall, winter and spring but a strong increase in summer precipitation, which will be discussed more below.

California is climatologically dry in the summer, so the large percentage increases found at that time (Fig. 10d) represent small amounts. This is brought out in Fig. 11, where the size of the circles indicates the climatological precipitation in each region over the historical period (1985-1994), and each wedge shows what fraction of the total annual precipitation falls in that season. Although Fig. 10d demonstrates that the percentage increases in JJA precipitation are substantial, Fig. 11c shows that summer precipitation makes up only a small fraction of annual precipitation in all regions except the Anza-Borrego (extreme Southeast corner of the state).

a) Forced changes versus natural internal climate variability

Figure 6 showed that projected temperature changes tend to be as large, or larger than, the 90% confidence interval of natural internal variability. This is not true for precipitation (Fig. 12). The blue bars (90% confidence interval of natural variability) tend to be an order of magnitude larger than the mean model changes (green bars). At the same time, the spread across the models (red lines) is typically larger

than the mean model change, except for the JJA drying signal across the northern part of the state (Fig. 12d). The spread of precipitation projections across models should be kept in mind when evaluating the results described below. In practical terms, this means that anthropogenic forcing will have only incremental effects on yearly-averaged precipitation over most of the state. However even precipitation shifts small compared to the inter-seasonal or inter-annual variability can be important for the long term water balance of a region, especially where the water supply has little room for reduction. For example, California droughts can last 5-10 years, a long enough averaging period to reduce natural variability sufficiently to expose small but systematic precipitation shifts.

b) The influence of downscaling technique

The effect of downscaling technique on precipitation must be interpreted cautiously, since not all models were downscaled with all techniques. The global models downscaled with a daily technique (either dynamical or BCCA) happened to be drier than the average global model by about 10 percentage points in the annual average (Fig. 13a vs. Fig 13b). The precipitation changes in the dynamical and BCCA downscaled fields are shown in Fig. 13c. Comparing Fig. 13c to Fig. 13b shows that the tendency of the BCCA and dynamical downscaling has been to make the simulation wetter in all regions. In the monsoon-influenced region in the southeast of the state, the wettening tendency of BCCA and dynamical downscaling is so strong, an increase in precipitation is projected even though the global models that had daily data showed more than average drying in that region.

The difference between downscaling techniques can be better isolated by using a single global model at a time. Figure 14 shows the yearly precipitation change (%) simulated by the different downscaling techniques applied to the GFDL 2.1 and CCSM3 global model runs, along with the global fields for comparison. The downscaling methods all gave similar results for temperature (Fig. 4). However the agreement depends on the global model for precipitation. The top row of Fig. 14 shows the different downscaling techniques give similar results when applied to the GFDL 2.1 global model. Both

statistical methods tend to be more faithful to the projected changes of the driving GCM than the dynamical models, as expected. However the bottom row of Fig. 14 shows that different downscaling methods give quite different results for CCSM3 (i.e., Fig. 14g vs. Fig. 14j), with the statistical methods again being most similar to the global GCM signal. Our experience has been that applications experts using climate projections tend to believe that dynamically downscaled results must be the best, yet in the Southeastern part of the state, Fig. 14i shows CCSM3/WRF projects a 26% drying while CCSM3/RSM projects 23% wetter conditions (Fig. 14j). How are these results to be understood?

The diversity of responses in CCSM3 can be understood, in large part, by considering the details of precipitation changes in each season (Fig. 15). Figures 15a and 15b show the statistical methods applied to CCSM3, while Figs. 15c and 15d show the dynamical methods. Each panel shows the regions in roughly geographical order, and each region has a set of 4 bars showing the climatological seasonal precipitation (DJF, MAM, JJA, and SON, counting the bars from left to right) and the change in precipitation projected by the downscaling technique (colored portion of the bars). Both dynamical methods show 20-30% precipitation increases in winter, while the statistical methods show increases of less than 10%. Both statistical methods show MAM and SON drying of 20-30%, while the dynamical methods show drying of <10%. In other words, the statistical and dynamical downscaling technique are showing the same patterns, but with different weighting by season. Depending on how the oppositely-signed tendencies are weighted, the yearly average difference can be positive or negative.

The dynamically downscaled results have the ability to develop trends different from those found in the original global model. In theory this is fine because the GCMs do not resolve the topography, which affects precipitation. The problem is, however, that the statistical and dynamical results suggest different trends, and the dynamical trends do not agree even given the same GCM forcing. What determines the differences between a global model trend and the corresponding dynamically downscaled trend? Is it as simple as, say, WRF always projecting summers that show more exaggerated drying than found in the global model?

This is addressed in Fig. 16, which shows a selection (DJF and JJA) of seasonally downscaled fields driven by the GFDL and CCSM3 global models. The values plotted are the differences (percentage points) between the dynamically downscaled precipitation changes and the changes found in the original global model. In other words, they are differences of differences, and show not the future precipitation changes, but rather how dynamical downscaling alters the original global model trends. Although we are limited by having only a small selection of results, some patterns are evident. For example, in DJF, all three downscaled fields using the GFDL model look similar to each other (16a, 16e, 16i), and both available dynamically downscaled fields using the CCSM3 model look similar to each other (16c, 16g), but the GFDL results do not look like the CCSM3 results. This suggests that in DJF, the effect of dynamical downscaling is influenced primarily by the global model characteristics (e.g., the large-scale atmospheric circulation), and is less sensitive to the particular dynamical downscaling model used.

On the other hand, in summer, in the southern half of the state, RSM (16f, 16h) tends show much wetter changes than the global models (either GFDL or CCSM3), while WRF (16b, 16d) shows much drier changes than the global models (either GFDL or CCSM3). The changes produced by RegCM3 lie in between (16j). This indicates that summer precipitation, which presumably is less dominated by global circulation and contains a larger regional influence, is influenced more by the particular parameterizations used by an individual dynamical downscaling model than by the global driving model.

c) Changes in daily precipitation

Three-day accumulations of precipitation can be used to understand the potential for flooding (Das et al. 2011), as it typically takes a few days for the soil to saturate during storm. When examining daily time scales we again use data pooled across only the BCCA and dynamical downscaling techniques, since BCSD reconstructs daily time sequences from historical analog months. This includes data from the CCSM3, GFDL 2.1, PCM1, and CNRM CM3 global models (Table 1).

The distributions of the maximum three-day accumulation in a calendar year are shown in Fig. 17. Nearly all of California shows striking increases in maximum three-day accumulations, in many instances generating values far outside the historical distribution. Similar results were found in Kim (2005), although that work considered snow/rain distinctions that we are not examining here. Along the Northern coast, the historical distribution tops out at 80 mm/day with a 0.01/year chance. In the future, that same value has a greater than 0.1/year chance, and the distribution now extends up to 120 mm/day. At the same time, the low-precipitation end of the distribution is extended as well. In other words, the models project a tendency towards a wider span of variability along with the pronounced increase in maximum 3-day accumulations.

d) Storm intensity versus frequency

We have seen that various changes in seasonal precipitation are projected by the 2060s (albeit with significant variability, both natural and across models). Do these arise from changes in the frequency of storms or their intensity?

To address this, we must first be able to identify a "stormy" day (i.e., one with non-zero precipitation). Since we are considering precipitation averages over regions, this is not straightforward (e.g., Chen and Knutson, 2008). The larger the averaging area, the more likely it is that a storm will be encountered somewhere, so the incidence of zero-precipitation days will be lower than found at stations within the region. This is related to the problem that coarse-resolution GCMs have with predicting a large number of days with a small amount of drizzle (e.g., Sun et al. 2006, Dai 2006). We address this problem by defining a threshold > 0, above which we consider a region to be experiencing a day with precipitation. Details on picking the threshold, and a validation against observations, are given in Appendix 1. Days with precipitation greater than the threshold will be termed "rainy" days.

Figure 18 shows (for 4 representative regions) the change in precipitation by month (top row), change in the number of rainy days (middle row), and percentiles of precipitation on rainy days (bottom

row). Again, only BCCA and dynamically downscaled data have been used in this analysis, since those are driven by daily global model data. (In a sensitivity test we recomputed this figure using BCCA data, and found little difference except in summer in the North American monsoon region, where BCCA does not show the pronounced wettening.) Virtually the entire state has a statistically significant drop in spring precipitation, particularly in April. In all regions this is accompanied by a decrease in the number of rainy days, although this decrease is not always statistically significant. This pattern is repeated, although more weakly, in the autumn: most regions show a decrease in precipitation that is associated with a decrease in the number of rainy days.

Most of the regions, with the exception of the Anza-Borrego, show a tendency towards increasing 95th percentile precipitation during some or all of the cold season months (Nov-Mar; bottom row of Fig. 18). This increase in heavy precipitation events accounts for the generally heavier winter precipitation (e.g., Fig. 10b), since there are generally modest decreases in the number of rainy days (Fig. 18), particularly in December. In other words, winter average precipitation increases despite fewer rainy days because precipitation events intensify.

Although this result is obtained with data pooled across the BCCA and dynamical downscaling techniques, the spread across models shown in Fig. 12 makes it perhaps unsurprising that the models do not all agree on this result. Of the four models with daily data (CCSM3, GFDL 2.1, PCM1, and CNRM CM3), CCSM3 shows the strongest increase in winter precipitation intensity. GFDL 2.1 and PCM1 show weaker increases in intensity along the coast and decreases in the far Northeast, while CNRM shows mild decreases in storm intensity (and winter drying of 8-45%, mostly due to fewer days with precipitation) throughout the state.

The Anza-Borrego (Fig. 18) and Inland Empire regions (not shown), which are affected by the North American monsoon, experience an increase in summer (JJA) precipitation that is associated with both an increase in the number of rainy days and increase in the median precipitation. Because of the spread of responses across the models, these changes are not statistically significant. CCSM3 and GFDL

show these increases strongly, while CNRM shows only a weak increase and PCM shows a slight decrease.

The overall effect of changes in storm intensity vs. frequency in the pooled daily data is shown in Fig. 19, by season and region. In contrast to Fig. 18, which showed each quantity in its native units (i.e., number of rainy days and percentiles of precipitation), Fig. 19 expresses the change in number of rainy days and storm intensity in terms of the impact the changes have on total seasonal precipitation (cm). To make this conversion, the problem is linearized by assuming that each additional rainy day in the future increases the total seasonal precipitation by an amount equal to the average rainy-day precipitation in the historical period (likewise for the loss of a rainy day decreasing the seasonal precipitation). The effects of changes in storm intensity are then calculated as the actual change in seasonal precipitation minus the contribution due to the change in number of rainy days. As a result, each region's change in future precipitation (leftmost bars in Fig. 19, colored green for wet and brown for dry) is equal to the sum of changes arising from changes in the number of rainy days (middle bars in Fig. 19, yellow for less rainy days and grey for more) and storm intensity (rightmost bars in Fig. 19, red for more intensity and blue for less).

Several patterns can be seen in Fig. 19. Averaged across the available daily data, almost all locations and seasons show an increase in storm intensity, except for winter in the south of the state. At the same time, almost all locations and seasons show a decrease in the number of precipitating days, except for the southeastern part of the state in summer. The way these two opposing tendencies combine yields a complex pattern of seasonal precipitation changes. In the northern part of the state in winter, the increase in storm intensity is stronger than the decrease in number of precipitating days, resulting in an overall mild (3-6%) increase in seasonal precipitation. In spring (MAM) a mild increase in storm intensity coupled with a strong decrease in number of precipitating days yields a significant drying tendency (> 10%). This can also be seen in autumn (SON), although the changes in storm intensity are small in this season. Finally, the southeastern part of California, on the edge of the region affected by the North

American monsoon, shows both a mild increase in storm intensity and strong increase in number of precipitating days in summer (JJA), resulting in large (> 100%) increases in that season's precipitation.

3.3 Joint distributions of temperature and precipitation change

For planning purposes it can be useful to know whether the distributions of temperature and precipitation change are related. For example, perhaps the warmest projections are also the driest. Figure 20 shows two-dimensional distributions of temperature (x-axis) and precipitation (y-axis) changes in winter, which generally experiences the largest share of precipitation in California. The data has been re-sampled as in Dettinger (2005), described above. We find no evidence that the temperature and precipitation distributions are linked, either in winter (Fig. 20) or the other seasons (not shown). The most notable feature of Fig. 20 is that the temperature distributions are well separated from zero, while the precipitation distributions essentially straddle the zero line (cf. Fig. 6 vs. Fig. 12).

4. Summary and Conclusions

Our purpose has been to present probabilistic projections of temperature (T) and precipitation (P) changes in California by the 2060s. We have emphasized daily distributions, since a number of important applications in energy demand, water management, and agriculture require daily information. Similarly, we focused on probabilistic estimates and included natural internal climate variability, because it is useful for planners to understand the range of climate projections and how those compare to natural climate fluctuations.

We downscaled data from 16 global models using a combination of two statistical techniques (BCSD and BCCA) and three nested regional climate models (WRF, RCM, and RegCM3), although not all GCMs were downscaled with all techniques. Due to computational constraints, we have dynamically downscaled results for only a historical (1985-1994) and future (2060-2069) period, and one emissions scenario, SRES A2. The 2060s is about the last decade that does not show a clear separation between the

A2, B1, and A1B emissions scenarios, but including the uncertainty in how humans might respond to climate change would certainly widen the future T and P distributions.

As appropriate given our focus on applications, all model output was bias corrected. The GCM data was bias corrected before being statistically downscaled, while the dynamically downscaled data was bias corrected after it was produced. We find:

- January-averaged temperatures as cold as any found in the historical period are still seen in the 2060s, although rarer. However Januarys warmer than any found in the historical period are seen about 20% of the time. By contrast, cold Julys (judging by historical standards) all but disappear by the 2060s, and the hottest July average temperature found in any simulation's historical period becomes a moderately cool event (15-40th percentile) by the 2060s.

- Similar to previous studies (e.g., Leung et al. 2004, Coquard et al. 2004, Hayhoe et al. 2004, Duffy et al. 2006) the projected warming is more consistent across models and regions than the projected P change, which varies in sign by model. Also, the warming is greater in the inland regions and in summer, with the greatest warming in the Northeast of California in the summer.

- The downscaled T projections tend to agree across downscaling techniques, except for BCCA, which shows smaller trends than the other techniques or original GCM for reasons related to the way the bias correction works.

- Year-to-year variability in seasonally averaged T is about twice as large as the mean seasonal climate change warming in winter, and about half the mean warming in summer. In either season, the model range in projected warming is about half the mean warming signal.

- Distributions of July daily maximum T shift more or less uniformly towards warmer values, except along the Northern coast, where maximum values are little changed from

today. In January, by contrast, the distributions are little changed below the median, but show a shift towards a greater incidence of a few particularly warm days.

- Distributions of the warmest 3-day average T, which drive air conditioner demand, show approximately uniform shifts of +2 C across the distribution.

- Averaged across all models and downscaling techniques, weak annual mean drying is found in the southern part of the state, and near zero P change in the northern part of the state. The disagreement across models is large, however. The seasonal signal is more complicated; winters tend to become wetter in the north, spring and autumn show strong drying, and summer (when the actual values of P are quite small) shows drying in the north but wetter conditions in the south. Year-to-year natural variability is typically more than an order of magnitude greater than these changes, and the range of projections across models includes zero, except in summer and the southern part of the state in spring. Because natural variability in precipitation is large compared to the anthropogenic change, future work using time slices longer than the 10-yr periods available here would be valuable.

- The different downscaling techniques agree less with P than they do with T. This is due to the annual P change in most models being made up of competing effects, with winter wettening and spring/autumn drying. Different models and downscaling techniques end up weighting these competing seasonal effects differently, which can result in a positive or negative change in the yearly average.

- The dynamical downscaling techniques show larger increases in summer P in the region affected by the North American monsoon than found with the statistical downscaling techniques. Regional dynamical models are able to amplify monsoon effects that are only coarsely represented by the GCM's, but statistical downscaling has no way to sharpen these features. In general, the winter P response seems more sensitive to which GCM

was used, while the summer P response seems more sensitive to which RCM was used. A similar finding was reported in Pan et al. (2001).

- There is a substantial increase in 3-day maximum precipitation, with peak values increasing 10-50%, in agreement with Kim (2005). The increases are largest in the northern part of the state, where values that have only a 0.01 probability of occurrence in the historical period become 10 times more likely by the 2060s.

- Changes in seasonal P are determined by a competition between generally increasing storm intensity (mean P on days when P occurs) and generally decreasing number of stormy days (days when P occurs). Winter P increases in the northern part of the state are driven by significant increases in storm intensity with only mild decreases in the number of stormy days, while the spring and autumn drying are driven by large decreases in stormy days with only mild increases in storm intensity. The region influenced by the North American monsoon (the extreme southeast of the state) shows an increase in both stormy days and storm intensity in summer.

We believe these results will help planners better adapt to the changes in climate that are in store for the western U.S.

Acknowledgements

Appendix 1. Calculating "zero-precipitation" days.

We want to compute how the number of days with precipitation (P) changes in the future and the mean P on those days. However, GCM grid cell precipitation values are area averages, which do not correspond to station measurements (Chen and Knutson, 2008). This can be seen in the way current GCMs over-predict the number of days with a small amount of precipitation (e.g., Sun et al. 2006, Dai 2006; cf. Wehner et al. 2010). These problems are seen in the downscaled P data as well, albeit to a lesser extent. For these reasons, defining a model's "zero-precipitation day" as one with precipitation identically equal to zero gives discrepancies with station-based estimates of the frequency of zero-precipitation days.

Earlier studies have addressed this problem by defining a threshold > 0, below which a model is considered to have zero precipitation. For example, Leung et al. (2004) used 0.01 mm/day, Kim (2005) used 0.5 mm/day, and Caldwell et al. (2009) used 0.1 mm/day. Given this range, which is influenced by the size of the model gridcell and the region's precipitation characteristics, how can we sensibly choose a zero-precipitation threshold for the model values?

Our model data is bias-corrected, which means the model mean P values are uniform and equal to observed, so we can sensibly pool all the historical model P data without being concerned that different models will contribute wildly different mean values. Let P_z^{mod} be the zero-precipitation threshold we seek for the pooled model data, and P_z^{obs} be the zero-precipitation threshold for the observations (which is always zero). Let $f_z(P)$ be the fraction of days with $P <= P_z$ for either the model or observations. We choose P_z^{mod} such that $< f_z^{obs}(P^{obs}) > = f_z^{\mathrm{mod}}(< P^{\mathrm{mod}} >)$, where the angle brackets $(<>)$ indicate area averaging over one of our California analysis regions. In other words, we choose a zero-precipitation threshold that makes the fraction of zero-precipitation days calculated from the pooled model data's precipitation averaged over the region equal to the regionally-averaged fraction of zero-precipitation days calculated from the observations. In this calculation we use the precipitation values from Hamlet and Lettenmier (2005) as our observations, which are based on NOAA's co-operative observational network,

but have gridded values across our entire domain, with high altitude values interpolated by taking into account the effects of elevation.

Figure 21 illustrates the process of choosing P_z^{mod}. Figures 21a and 21b show the region-averaged climatological percent of zero-precipitation days from the Hamlet and Lettenmier (2005) observations for December and July, respectively. The northwest coastal region has the lowest number of zero-precipitation days in December, while the Anza-Borrego region has the highest. In July, at least 85% of the days have zero precipitation in every region.

Figure 21c shows how the climatological number of zero-precipitation days in the pooled model data varies with P_z (black curve) in one particular month and region (Sacramento and the Central Valley in December). As expected, the fraction of zero-precipitation days increases as P_z increases. About 25% of days have zero precipitation when using the threshold $P_z^{\text{mod}} = 0$, compared to 60% of the days in the observations (red line in Fig. 21c). When $P_z^{\text{mod}} = 0.25$ mm/day (blue line in Fig. 21c), the number of zero precipitation days in the pooled model data equals that found in the observations. This is referred to as the "best-match cutoff".

Figure 21d shows the best-match cutoff for all regions and months. Two outlier regions can be seen: the Sierra Nevada (red), and the Anza-Borrego (blue). The best-match cutoff is influenced by such factors as the size of the region, and the mean and spatial coherence of precipitation in the region. For the outliers the mean precipitation clearly plays a factor, as the Sierra Nevada is one of the highest-precipitation regions and the Anza-Borrego is the lowest.

Although Fig. 21d shows the best-match cutoffs, there are 132 values, one for each of the 11 regions and 12 months. Using all 132 values is complex and raises the specter of over fitting. Various options are possible, such as choosing values by region, month, or some combination thereof. Based on the pronounced seasonal cycle all regions undergo, we decided to choose two values of P_z^{mod}, one for the dry summer months and one for the rest of the year. Figure 21e shows the data from 21d averaged across

all regions each month. We use the regionally-averaged best-match cutoff of 0.36 mm/day in June-July-August (JJA; red line in Fig. 21e), and 0.71 mm/day in the rest of the year (blue lines in Fig. 21e).

How well the behavior of the full 132 values is reproduced by using just these two values is shown in Fig. 21f, a scatterplot of the observed climatological percent of zero-precipitation days for each month and region (x axis) vs. the model value computed using just the two cutoff values (y axis). The regression line (blue) has $r^2 = 0.92$, so we consider this a satisfactory and physically reasonable solution to the problem of computing the number of "zero-precipitation" days in the models.

As a sensitivity test of our results to the selection of the cutoff values, we repeated the analysis shown in the main text (Figs. 18 and 19) with the full set of 132 values. The differences were minor, which gives us confidence that this selection is not unduly affecting our conclusions. We note that the spread across models in the quantities shown in Fig. 18 tends to be large in comparison to the errors shown in Fig. 21f.

References

Abatzoglou JT, Redmond KT, Edwards LM (2009) Classification of Regional Climate Variability in the State of California. J App Meteor Clim 48:1527-1541

AchutaRao K, Sperber KR (2006) ENSO simulation in coupled ocean-atmosphere models: are the current models better? Clim Dyn 27:1-15

Anderson, J., F. Chung, M. Anderson, L. Brekke, D. Easton, M. Ejeta, R. Peterson and R. Snyder, 2008. Progress on incorporating climate change into management of California's water resources. *Climatic Change* **87 (Suppl 1)**:S91–S108, DOI 110.1007/s10584-10007-19353-10581.

Barnett TP, Pierce DW, Hidalgo HG, Bonfils C and others (2008) Human-induced changes in the hydrology of the western United States. Science 319:1080-1083

Bell JL, Sloan LC, Snyder MA (2004) Regional changes in extreme climatic events: A future climate scenario. J Clim 17:81-87

Bonfils C, Santer BD, Pierce DW, Hidalgo HG, Bala G, Das T, Barnett TP, Cayan DR, Doutriaux C, Wood AW, Mirin A, Nozawa T (2008) Detection and Attribution of Temperature Changes in the Mountainous Western United States. J Clim 21:6404-6424

Brekke LD, Miller NL, Bashford KE, Quinn NWT, Dracup JA (2004) Climate change impacts uncertainty for water resources in the San Joaquin River Basin, California. J Amer Water Res Assoc 40:149-164

Brekke, L. D., M. D. Dettinger, E. P. Maurer, and M. Anderson (2008), Significance of model credibility in estimating climate projection distributions for regional hydroclimatological risk assessments, Climatic Change, 89(3-4), 371-394, doi: 310.1007/s10584-10007-19388-10583.

Brekke, L. D., E. P. Maurer, J. D. Anderson, M. D. Dettinger, E. S. Townsley, A. Harrison, and T. Pruitt (2009), Assessing reservoir operations risk under climate change, Water Resour. Res., 45, W04411, doi:10.1029/2008WR006941.

Caldwell P, Chin HNS, Bader DC, Bala G (2009) Evaluation of a WRF dynamical downscaling simulation over California. Clim Change 95:499-521

Cayan, D. R., 1996. Interannual climate variability and snowpack in the western United States. *J. Climate* **9**:928-948.

Cayan D, Leurs AL, Hanemann M, Granco G, Croes B (2006) Scenarios of climate change in California: An overview. California Climate Change Center report CEC-500-2005-186-SF. 53 pp.

Chen CT, Knutson T (2008) On the verification and comparison of extreme rainfall indices from climate models. J Clim 21:1605-1621.

Chin HNS, Caldwell PM, Bader DC (2010) Preliminary Study of California Wintertime Model Wet Bias. Mon Wea Rev 138:3556-3571

Christensen JH, Carter TR, Rummukainen M, Amanatidis G (2007) Evaluating the performance and utility of regional climate models: the PRUDENCE project. Clim Change 81:1-6

Christensen JH, Kjellstrom E, Giorgi F, Lenderink G, Rummukainen M (2010) Weight assignment in regional climate models. Clim Res 44:179-194

Collins M, An SI, Cai WJ, Ganachaud A and others (2010) The impact of global warming on the tropical Pacific ocean and El Nino. Nature Geosci 3:391-397

Coquard J, Duffy PB, Taylor KE, Iorio JP (2004) Present and future surface climate in the western USA as simulated by 15 global climate models. Clim Dyn 23:455-472

Dai A (2006) Precipitation characteristics in eighteen coupled climate models. J Clim 19:4605-4630.

Das, T., H. Hidalgo, D. Cayan, M. Dettinger, D. Pierce, C. Bonfils, T.P. Barnett, G. Bala and A. Mirin, 2009: Structure and origins of trends in hydrological measures over the western United States. *Journal of Hydrometeorology*, **10**, 871-892. doi:10.1175/2009JHM1095.1.

Das T., Dettinger M.D., Cayan D.R. and Hidalgo H.G., 2011: Potential increase in floods in Californian Sierra Nevada under future climate projections. *Climatic Change* (*in revision*).

Dettinger MD (2005) From climate-change spaghetti to climate-change distributions for 21st century California. San Francisco Estuary and watershed science. 3:issue 1, article 4. 14 pp.

Dettinger, M.D., and S. Culberson, 2008: Internalizing climate change - Scientific resource management and the climate change challenges. San Francisco Estuary and Watershed Science, **6**(2), Article 6.

Dickinson RE, Kennedy PJ, Henderson-Sellers A, Wilson M (1986) Biosphere-atmosphere transfer scheme (BATS) for the NCAR Community Climate Model, Tech. Rep. NCAR/TN-275+STR, National Center for Atmospheric Research

Dickinson RE, Errico RM, Giorgi F, Bates GT (1989) A regional climate model for the western United States. Clim Change 15:383-422

Dudhia J (1989) Numerical study of convection observed during the winter monsoon experiment using a mesoscale two-dimensional model. J Atmo Sci 46:3077-3107

Duffy PB, Arritt RW, Coquard J, Gutowski W, Han J, Iorio J, Kim J, Leung LR, Roads J, Zeledon E (2006) Simulations of present and future climates in the western United States with four nested regional climate models. J Clim 19:873-895

Fritsch JM, Chappell CF (1980) Numerical prediction of convectively driven mesoscale pressure systems. part I: Convective parameterization. J Atmos Sci 37:1722–1733

Giorgi F, Brodeur CS, Bates GT (1994) Regional climate-change scenarios over the United States produced with a nested regional climate model. J Clim 7:375-399

Giorgi F, Mearns LO (2002) Calculation of average, uncertainty range, and reliability of regional climate changes from AOGCM simulations via the "reliability ensemble averaging" (REA) method. J Clim 15:1141-1158

Giorgi F, Mearns LO (2003) Probability of regional climate change based on the Reliability Ensemble Averaging (REA) method. Geophys Res Lett 30

Giorgi F, Bi XQ, Qian Y (2003) Indirect vs. direct effects of anthropogenic sulfate on the climate of east asia as simulated with a regional coupled climate-chemistry/aerosol model. Clim Change 58:345–376

Grell G (1993) Prognostic evaluation of assumptions used by cumulus parameterizations. Mon Wea Rev 121:764–787

Hamlet AF, Lettenmaier DP (2005) Production of temporally consistent gridded precipitation and temperature fields for the continental United States. J Hydromet 6:330-336

Hawkins E, Sutton R (2009) The potential to narrow uncertainty in regional climate predictions. Bull Amer Met Soc, 90, p1095, doi: 10.1175/2009BAMS2607.1

Hay LE, Clark MP (2003) Use of statistically and dynamically downscaled atmospheric model output for hydrologic simulations in three mountainous basins in the western United States. J Hydrol 282:56-75.

Hayhoe K, Cayan D, Field CB, Frumhoff PC and others (2004) Emissions pathways, climate change, and impacts on California. Proc Nat Acad Sci 101:12422-12427

Hidalgo HG, Dettinger MD, Cayan DR (2008) Downscaling with Constructed Analogues: Daily precipitation and temperature fields over the Unites States. California Energy Commission technical report CEC-500-2007-123. 48 pp.

Hidalgo HG, Das T, Dettinger MD, Cayan DR, Pierce DW and others (2009) Detection and Attribution of Streamflow Timing Changes to Climate Change in the Western United States. J Clim 22:3838-3855

Holtslag, AAM, de Bruijn EIF, Pan H-L (1990) A high resolution air mass transformation model for short-range weather forecasting. Mon Wea Rev 118:1561–1575

Hong SY, Pan HL (1996) Nonlocal boundary layer vertical diffusion in a Medium-Range Forecast Model. Mon Wea Rev 124:2322-2339

Hong SY, Dudhia J, Chen SH (2004) A revised approach to ice microphysical processes for the bulk parameterization of clouds and precipitation. Mon Wea Rev 132:103-120

Iacobellis SF, Somerville RCJ (2000) Implications of microphysics for cloud-radiation parameterizations: Lessons from TOGA COARE. J Atmos Sci 57:161-183

IPCC (2007) Climate change 2007: The physical science basis. Working group I contribution to the fourth assessment report of the Intergovernmental Panel on Climate Change. Cambridge University Press, Cambridge, United Kingdom and New York, USA. 996 pp.

Kanamaru H, Kanamitsu M (2007) Scale-selective bias correction in a downscaling of global analysis using a regional model. Mon Wea Rev 135:334-350

Kanamitsu M, Ebisuzaki W, Woollen J, Yang SK and others (2002) NCEP-DOE AMIP-II reanalysis (R-2). Bull Am Met Soc 83:1631-1643

Kanamitsu M, Kanamaru H, Cui Y, Juang H (2005) Parallel implementation of the regional spectral atmospheric model. California Energy Commission technical report CEC-500-2005-014. www.energy.ca.gov/2005publications/CEC-500-2005-014/CEC-500-2005-014.

Kanamitsu M, Kanamaru H (2007) Fifty-seven-year California Reanalysis Downscaling at 10 km (CaRD10). Part I: System detail and validation with observations. J Clim 20:5553-5571

Kanamitsu M, Yoshimura K, Yhang Y-B, Hong S-Y (2010) Errors of interannual variability and trend in dynamical downscaling of Reanalysis, J. Geohpys. Res., 115, doi:10.1029/2009JD013511

Kim J (2001) A nested modeling study of elevation-dependent climate change signals in California induced by increased atmospheric CO2. Geophys Res Lett 28:2951-2954

Kim J (2005) A projection of the effects of the climate change induced by increased CO2 on extreme hydrologic events in the western US. Clim Change 68:153-168

Kjellstrom E, Giorgi F (2010) Regional Climate Model evaluation and weighting Introduction. Clim Res 44:117-119

Knutti R, Furrer R, Tebaldi C, Cermak J, Meehl GA (2010) Challenges in Combining Projections from Multiple Climate Models. J Clim 23:2739-2758

Lebassi, B., J. González, D. Fabris, E. Maurer, N. Miller, C. Milesi, P. Switzer and R. Bornstein, 2009. Observed 1970–2005 Cooling of Summer Daytime Temperatures in Coastal California. *J. Climate* **22**:3558-3573.

Leung LR, Ghan SJ (1999a) Pacific Northwest climate sensitivity simulated by a regional climate model driven by a GCM. Part I: Control simulations. J Clim 12:2010-2030

Leung LR, Ghan SJ (1999b) Pacific Northwest climate sensitivity simulated by a regional climate model driven by a GCM. Part II: 2xCO(2) simulations. J Climate 12:2031-2053

Leung LR, Qian Y, Bian XD, Washington WM, Han JG, Roads JO (2004) Mid-century ensemble regional climate change scenarios for the western United States. Clim Change 62:75-113

Liang XZ, Kunkel KE, Meehl GA, Jones RG, Wang JXL (2008) Regional climate models downscaling analysis of general circulation models present climate biases propagation into future change projections. Geophys Res Lett 35

Manning, L. J., J. W. Hall, H. J. Fowler, C. G. Kilsby, and C. Tebaldi (2009), Using probabilistic climate change information from a multimodel ensemble for water resources assessment, Water Resour. Res., 45, W11411, doi:10.1029/2007WR006674.

Maurer EP, Duffy PB (2005) Uncertainty in projections of streamflow changes due to climate change in California. Geophys Res Lett 32

Maurer EP (2007) Uncertainty in hydrologic impacts of climate change in the Sierra Nevada, California, under two emissions scenarios. Clim Change 82:309-325

Maurer, E.P., I.T. Stewart, C. Bonfils, P.B. Duffy, and D. Cayan, 2007, Detection, attribution, and sensitivity of trends toward earlier streamflow in the Sierra Nevada, *J. Geophysical Research* 112, D11118, doi:10.1029/2006JD008088.

Maurer, E.P., H.G. Hidalgo, T. Das, M.D. Dettinger and D.R. Cayan, 2010: The utility of daily large-scale climate data in the assessment of climate change impacts on daily streamflow in California. Hydrol. Earth Syst. Sci., **14**, 1125-1138, doi:10.5194/hess-14-1125-2010.

Meehl GA, Covey C, Delworth T, Latif M and others (2007) The WCRP CMIP3 multimodel dataset - A new era in climate change research. Bull Am Met Soc 88:1383

Meehl GA, Hu AX, Santer BD (2009) The Mid-1970s Climate Shift in the Pacific and the Relative Roles of Forced versus Inherent Decadal Variability. J Clim 22:780-792

Mellor GL, Yamada T (1982) Development of a turbulence closure-model for geophysical fluid problems. Rev Geophys 20:851-875

Miller NL, Jin J, Schlegel NJ, Snyder MA and others (2009) An analysis of simulated California climate using multiple dynamical and statistical techniques. California Energy Commission report CEC-500-2009-017-F, August, 2009. 47 pp.

Mlawer EJ, Taubman SJ, Brown PD, Iacono MJ, Clough SA (1997) Radiative transfer for inhomogeneous atmospheres: RRTM, a validated correlated-k model for the longwave. J Geophys Res Atmos 102:16663-16682

Oleson KW, Dai Y, Bonan G, Bosilovichm M and others (2004) Technical description of the community land model (CLM). NCAR Tech. note NCAR/TN-461+STR. 186 pp.

Pal JS, Giorgi F, Bi XQ, Elguindi N and others (2007) Regional climate modeling for the developing world - The ICTP RegCM3 and RegCNET. Bull Amer Met Soc 88:1395

Pan Z, Christensen JH, Arritt RW, Gutowski WJ, Takle ES, Otieno F (2001) Evaluation of uncertainties in regional climate change simulations. J Geophys Res Atmos 106:17735-17751

Pierce DW (2001) Distinguishing coupled ocean-atmosphere interactions from background noise in the North Pacific. Prog Oceanogr 49:331-352

Pierce DW, Barnett TP, Hidalgo HG, Das T and others (2008) Attribution of Declining Western US Snowpack to Human Effects. J Clim 21:6425-6444

Pierce DW, Barnett TP, Santer BD, Gleckler PJ (2009) Selecting global climate models for regional climate change studies. Proc Nat Acad Sci 106:8441-8446

Snyder MA, Bell JL, Sloan LC, Duffy PB, Govindasamy B (2002) Climate responses to a doubling of atmospheric carbon dioxide for a climatically vulnerable region. Geophys Res Lett 29:4

Snyder MA, Sloan LC (2005) Transient future climate over the western United States using a regional climate model. Earth Interactions 9

Sun Y, Solomon S, Dai A, Portmann RW (2006) How often does it rain? J Clim 19:916-934

Takle ES, Gutowski WJ, Arritt RW, Pan ZT and others (1999) Project to Intercompare Regional Climate Simulations (PIRCS): Description and initial results. J Geophysi Res Atmos 104:19443-19461

Tiedtke M (1993) Representation of clouds in large-scale models. Mon Wea Rev 121:3040-3061.

Vicuna S, Maurer EP, Joyce B, Dracup JA, Purkey D (2007) The sensitivity of California water resources to climate change scenarios. J Amer Water Res Assoc 43:482-498

Wehner MF, Smith RL, Bala G, Duffy P (2010) The effect of horizontal resolution on simulation of very extreme US precipitation events in a global atmosphere model. Clim Dyn 34:241-247

Wilkinson R, Clarke K, Goodchile M, Reichman J, Dozier J (eds) (2002) Preparing for a changing climate: The potential consequences of climate variability and change, California. A report of the California regional assessment group for the U.S. global change research program. 431 pp. www.ncgia.ucsb.edu/pubs/CA_Report.pdf

Wood AW, Maurer EP, Kumar A, Lettenmaier DP (2002) Long-range experimental hydrologic forecasting for the eastern United States. J Geophys Res Atmos 107 , doi:10.1029/2001jd000659

Wood AW, Leung LR, Sridhar V, Lettenmaier DP (2004) Hydrologic implications of dynamical and statistical approaches to downscaling climate model outputs. Clim Change 62:189-216

Yeh SW, Kug JS, Dewitte B, Kwon MH, Kirtman BP, Jin FF (2009) El Nino in a changing climate. Nature 461:511-U570

Zeng XB, Zhao M, Dickinson RE (1998) Intercomparison of bulk aerodynamic algorithms for the computation of sea surface fluxes using TOGA COARE and TAO data. J Clim 11:2628-2644

Table 1

GCM	Institution	BCSD	BCCA	WRF	RSM	RegCM3
BCCR BCM 2.0	Bjerknes Centre Clim. Res., Bergen, Norway	Y				
CCCMA CGCM3.1	Canadian Centre, Victoria, B.C., Canada	Y				
CNRM CM3	Meteo-France, Toulouse, France	Y	Y			
CSIRO MK3.0	CSIRO Atmos. Res., Melbourne, Australia	Y				
GFDL CM2.0	Geophys. Fluid Dyn. Lab, Princeton, NJ, USA	Y				
GFDL CM2.1	Geophys. Fluid Dyn. Lab, Princeton, NJ, USA	Y	Y	Y	Y	Y
GISS e_r	NASA/Goddard Inst. Space Studies, N.Y., USA	Y				
INMCM 3.0	Inst. Num. Mathematics, Moscow, Russia	Y				
IPSL CM4	Inst. Pierre Simon Laplace, Paris, France	Y				
MIROC 3.2 medres	Center Climate Sys. Res., Tokyo, Japan	Y				
MIUB ECHO-G	Meteor. Inst. U. Bonn, Bonn, Germany	Y				
MPI-ECHAM5	Max Planck Inst. Meteor., Hamburg, Germany	Y				
MRI CGCM2.3.2	Meteor. Res. Inst., Tsukuba, Ibaraki, Japan	Y				
NCAR CCSM3	Nat. Center Atmos. Res., Boulder, CO, USA	Y	Y	Y	Y	
NCAR PCM1	Nat. Center Atmos. Res., Boulder, CO, USA	Y	Y			
UKMO HadCM3	UK Met Office, Exeter, Devon, UK	Y				

Table 1. The global general circulation models (GCMs) used in this project, their originating institution, and the downscaling method(s) applied. BCSD: bias correction with spatial disaggregation; BCCA: bias correction with constructed analogues; WRF: weather research forecast model; RSM: regional spectral model; RegCM3: Regional climate model version 3.

Table 2

Statistic	NCAR CCSM3	CNRM CM3	NCAR PCM1	GFDL CM2.1
σ pre bias correction	0.84	0.66	0.49	0.73
σ post bias correction	0.67	0.85	0.50	0.60
ΔT pre bias correction	2.7	1.7	1.3	2.3
ΔT post bias correction	2.2	2.3	1.3	1.9

Table 2. An example of the effect of bias correction on the standard deviation (σ) of average daily July temperature (for a future period of 2040-2069) on the projected changes in temperature (ΔT) between the future period and a historic baseline of 1950-1999 for a single grid point located at latitude 39, longitude -121, over northern California.
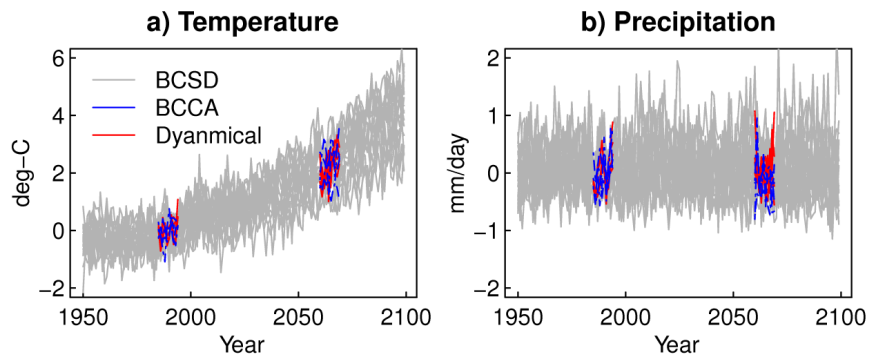
Figure 1. Left: temperature projections for the Sacramento/Central Valley region from all the model runs considered here, in deg-C relative to the historical period (1985-1994). Right: same, for precipitation in mm/day.
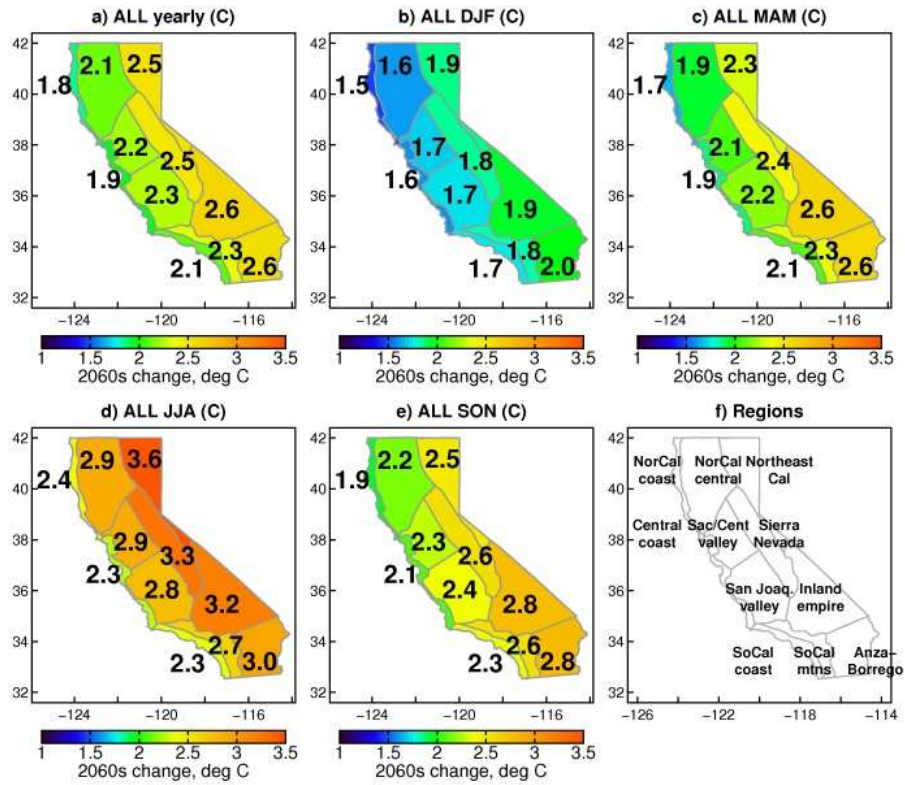
Figure 2. Mean temperature change (C) over the period 2060-69 minus mean over the period 1985-94. The averaged data from all models and downscaling techniques was averaged to generate the values. a) Yearly averaged values. b) through e): Dec-Jan-Feb, Mar-Apr-May, Jun-Jul-Aug, and Sep-Oct-Nov averages, respectively. f) The regions used in this work.

plot_CA_tracker_region_dels_v20.R.jpg
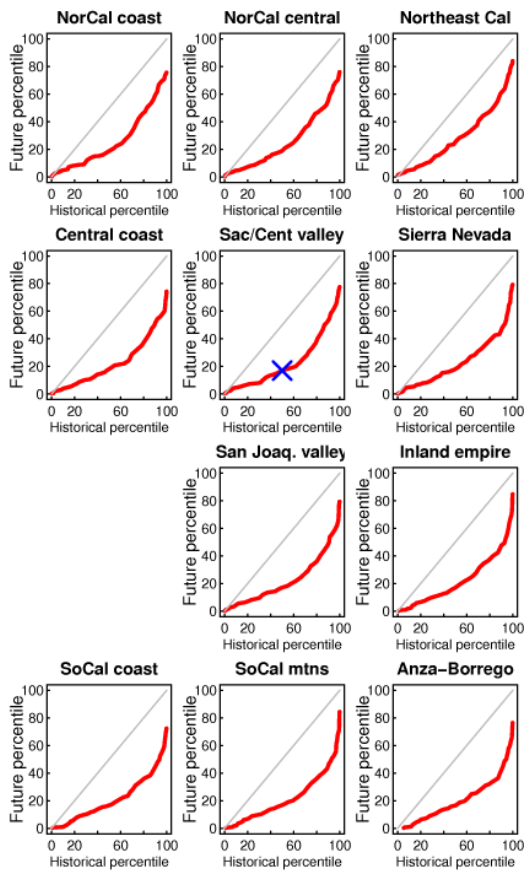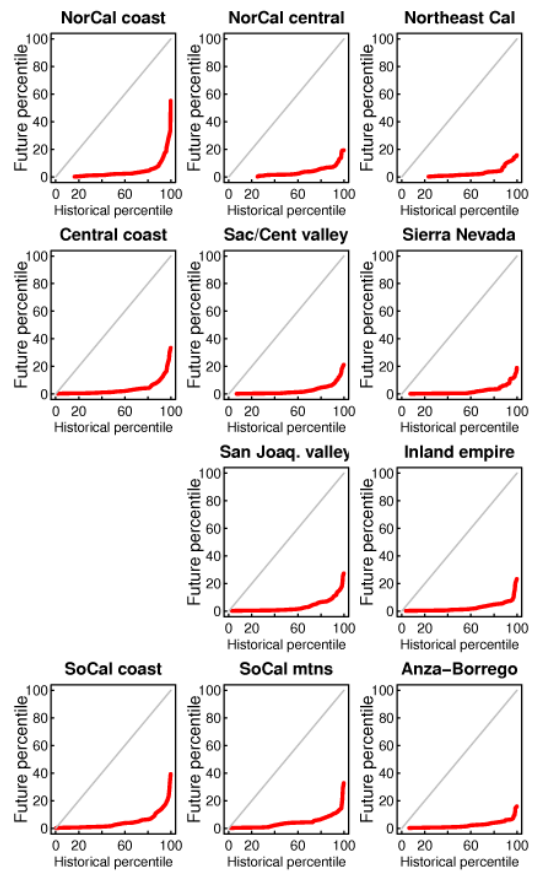
Figure 3. Correspondence between percentiles of monthly-averaged temperature in the historical period (x axis) and future period (y axis), for January (left) and July (right). For instance, the blue cross in panel a for the Sacramento/Central valley shows that the 50th percentile temperature in the historical period will become the 17th percentile value in the 2060s. The grey line shows what the result would be if there were no changes in the distributions. The regions are plotted in roughly geographic order (Northwest locations in the top left, etc.).

plot_change_monthly_prob_maps.R.01.gif
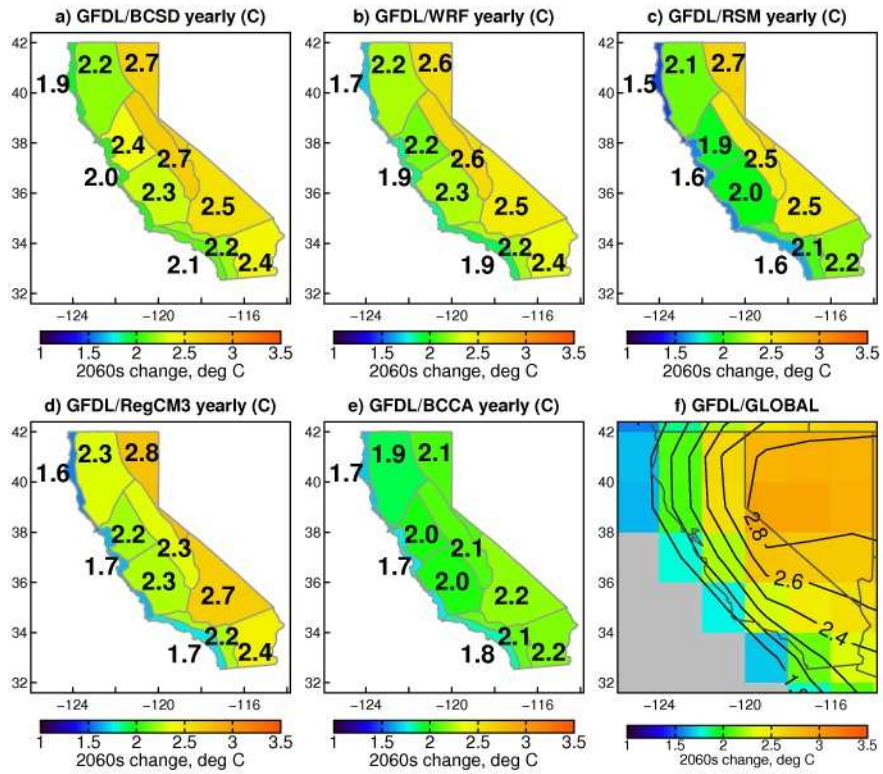
Figure 4. Yearly temperature change (C) (2060-2069 minus 1985-1994) from each downscaling technique applied to the GFDL 2.1 global model. The yearly temperature change from the global model is shown in panel f, for comparison.

plot_CA_tracker_region_dels_v21_gfdl_only.R.01.jpg

48
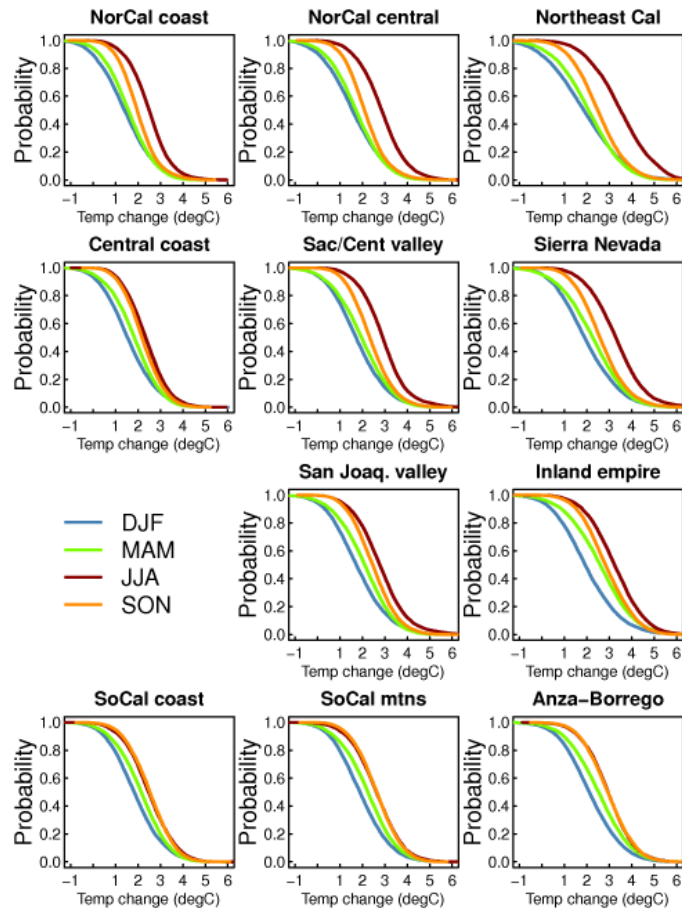
Figure 5. Probability of a temperature change of the indicated value or greater, by region and season. The regions are plotted in roughly geographic order (Northwest locations in the top left, etc.).
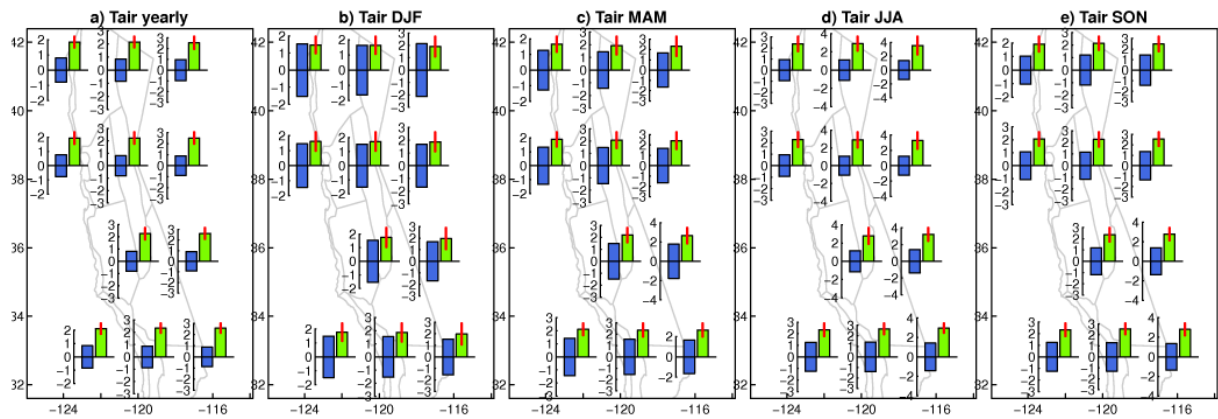
Figure 6. A comparison of the contribution of natural internal climate variability and model uncertainty to yearly and seasonally averaged projected temperature changes by the 2060s. Blue bars show the 90% confidence interval of natural internal climate variability in near surface air temperature (C) estimated across all models. Green bars show the mean model warming projected in the period 2060-69. The red line shows the 90% confidence interval in the projected warming across models. Note that each inset plot has a different scale for the Y axis, in degrees C.

make_dists_by_region_v2.R
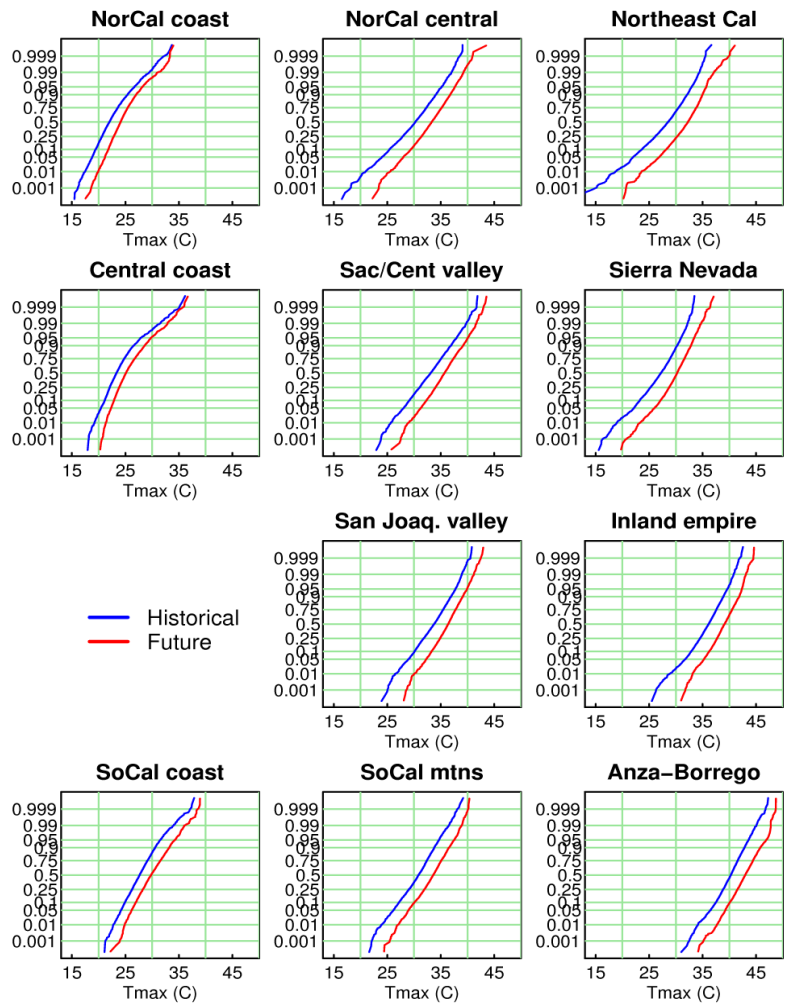
Figure 7. Cumulative distribution functions of July daily maximum temperature across the regions (plotted roughly geographically). The Y axis shows the probability (zero to one) of experiencing the indicated temperature or lower on any particular day in July. Results from the historical run are in blue; the future run is in red.

/merc02/pierce/data/cec_rcm/forcing/plot_monthly_cdfs_v2.R.07.ps
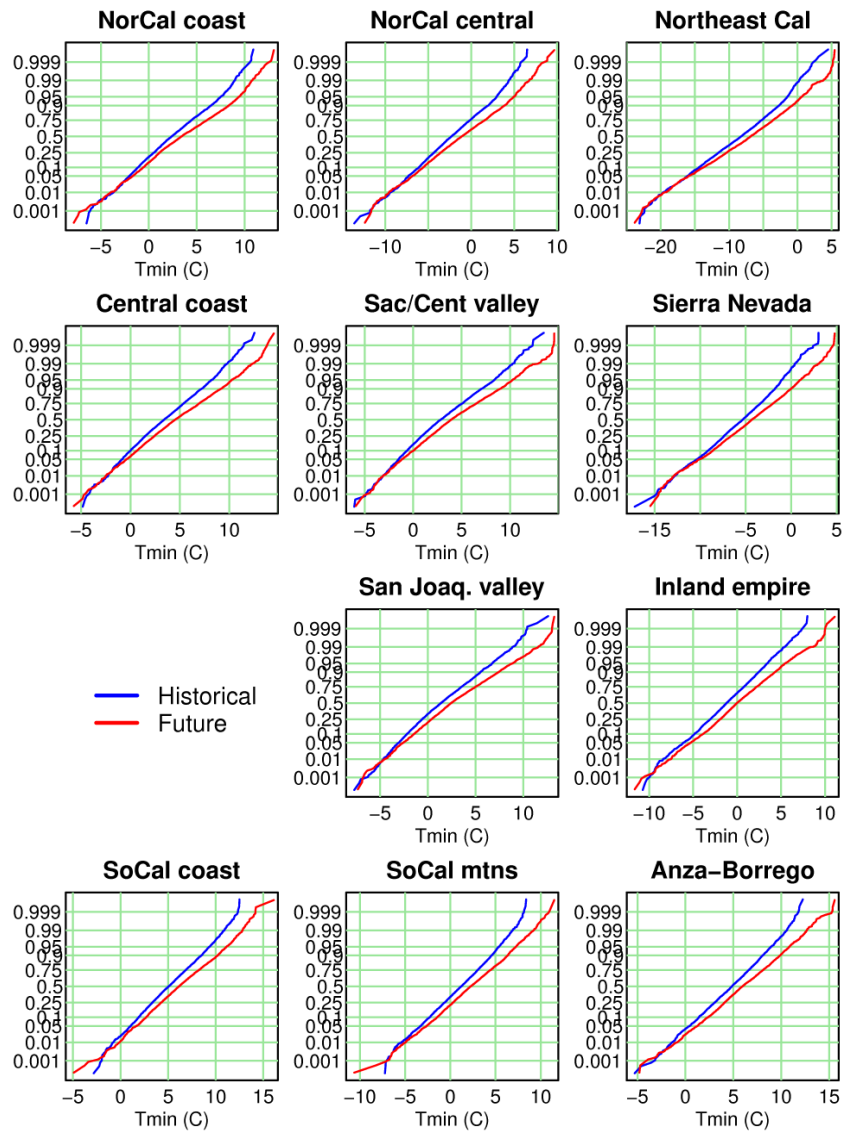
Figure 8. As Figure 7, but for January daily minimum temperatures.
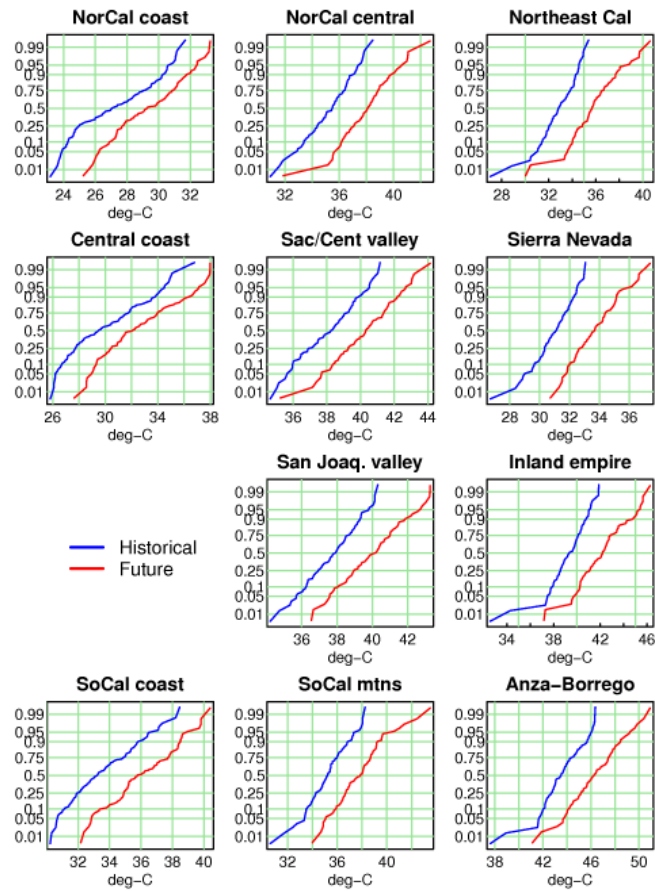
Figure 9. Cumulative distribution functions of the highest 3-day average temperature in the year. The Y axis shows the probability (zero to one) of having the warmest 3 days in a year be the indicated temperature or lower. Results from the historical run are in blue; the future run is in red. Panels are plotted roughly geographically.

/merc02/pierce/data/cec_rcm/forcing/plot_yearly_3daymax.R.ps
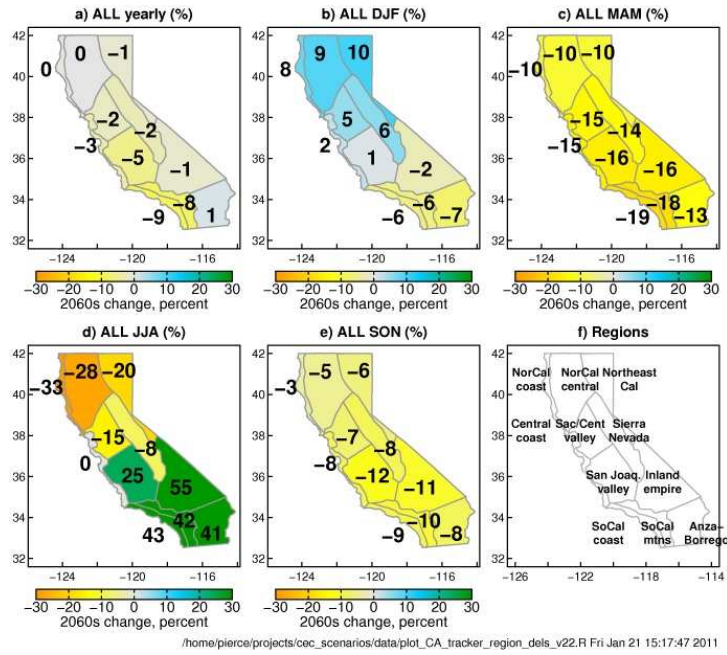
Figure 10. Precipitation change (%), mean over the period 2060-69 compared to mean over the period 1985-94. Data from all models and downscaling techniques was averaged to generate the values. a) Yearly averaged values. b) through e): Dec-Jan-Feb, Mar-Apr-May, Jun-Jul-Aug, and Sep-Oct-Nov averages, respectively. f) Regions used in this analysis.

plot_CA_tracker_region_dels_v22.R.02.jpg
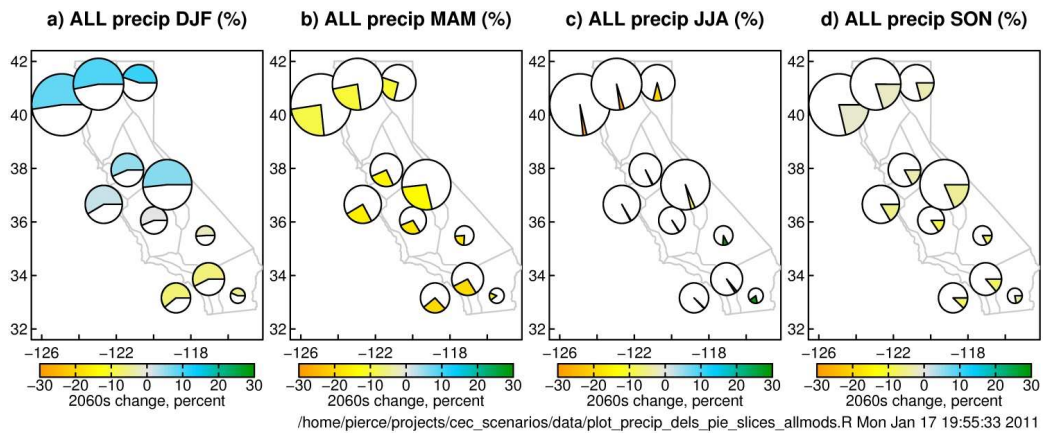
Figure 11. Changes in precipitation, mean in the future period (2060-69) compared to mean over the historical period (1985-94), averaged across all models and downscaling techniques. The area of each circle is proportional to the amount of yearly precipitation in that region in the historical period. The size of each pie wedge indicates the fraction of the total yearly precipitation that falls in that season. The color of each pie wedge indicates the precipitation change (%) experienced in that region and season (same as Fig. 8).

plot_precip_dels_pie_slices_allmods.R.gif
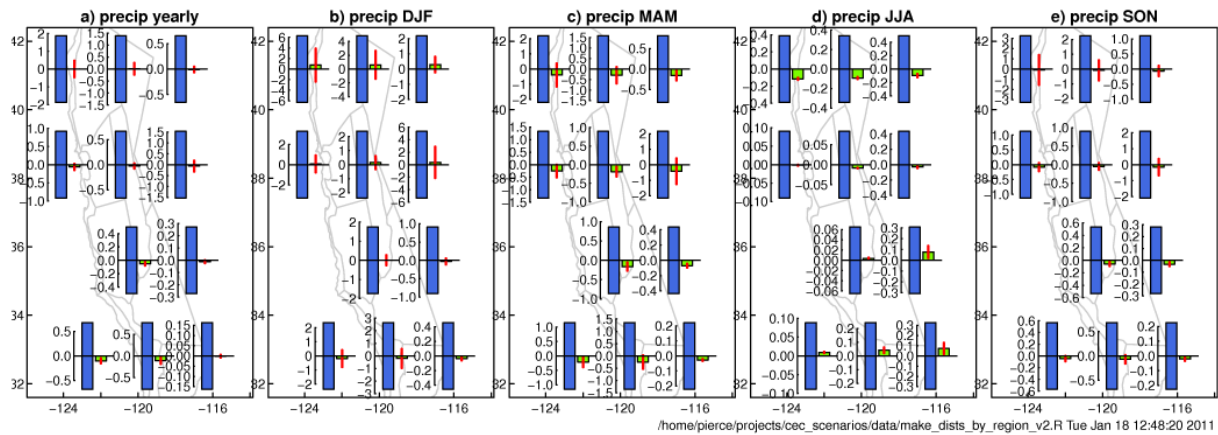
Figure 12. A comparison of the contribution of natural internal climate variability and model uncertainty to yearly and seasonally averaged precipitation changes. Blue bars show the 90% confidence interval of natural internal climate variability in seasonally averaged precipitation (mm/day) estimated across all models, for the period 2060-69. Green bars show the mean model precipitation change projected in the period 2060-69. The red line shows the 90% confidence interval in the projected precipitation change across models. Note that each inset plot has a different scale for the Y axis.

make_dists_by_region_v2.R
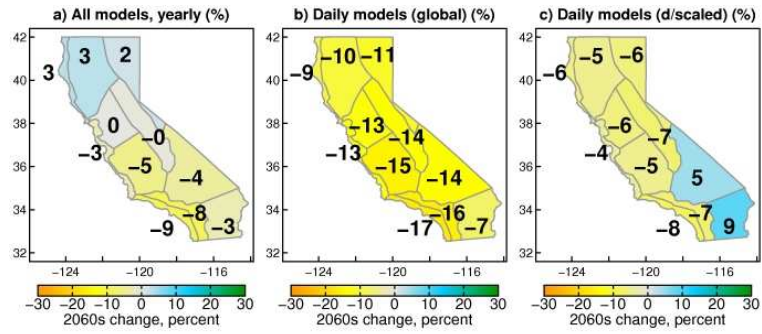
Figure 13. Yearly precipitation change (%, 2060-2069 compared to 1985-1994) for all the global models (panel a), the global models with daily data available (panel b), and the models with daily data available after downscaling with the BCCA or dynamical techniques (panel c).

plot_CA_tracker_region_dels_v21_technique_comparison.R.jpg
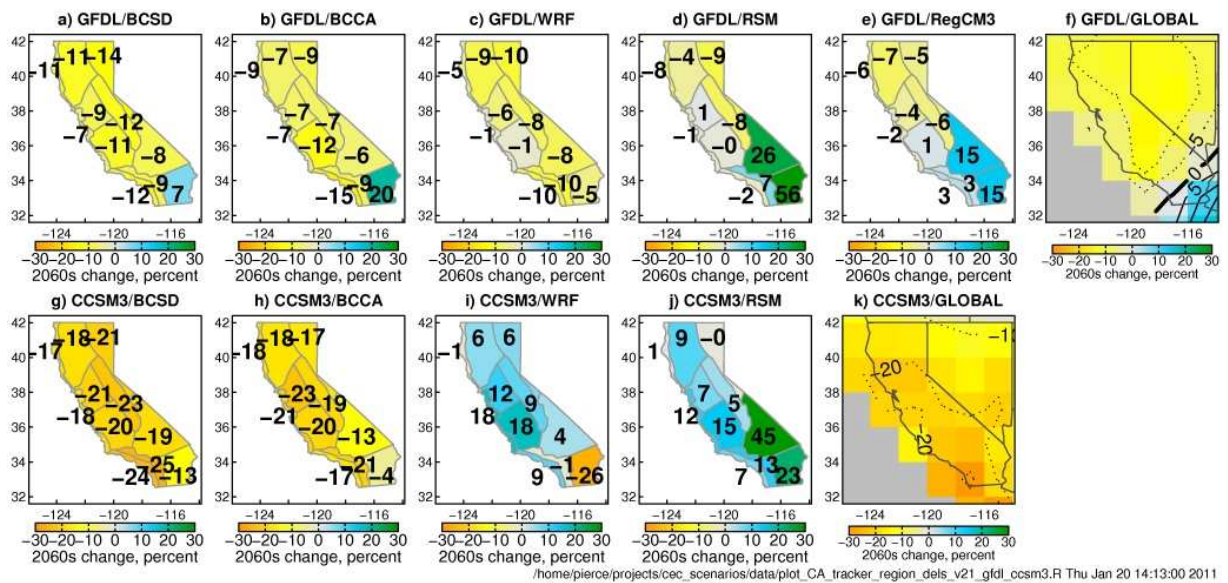
Figure 14. Yearly precipitation change (%, 2060-2069 compared to 1985-1994) from each downscaling technique applied to the GFDL 2.1 (top row) and CCSM3 (bottom row) global models. The yearly precipitation changes from the global models are shown in panels f and k, for comparison.

plotCA_tracker_region_dels_v21_gfdl_ccsm3.R.jpg
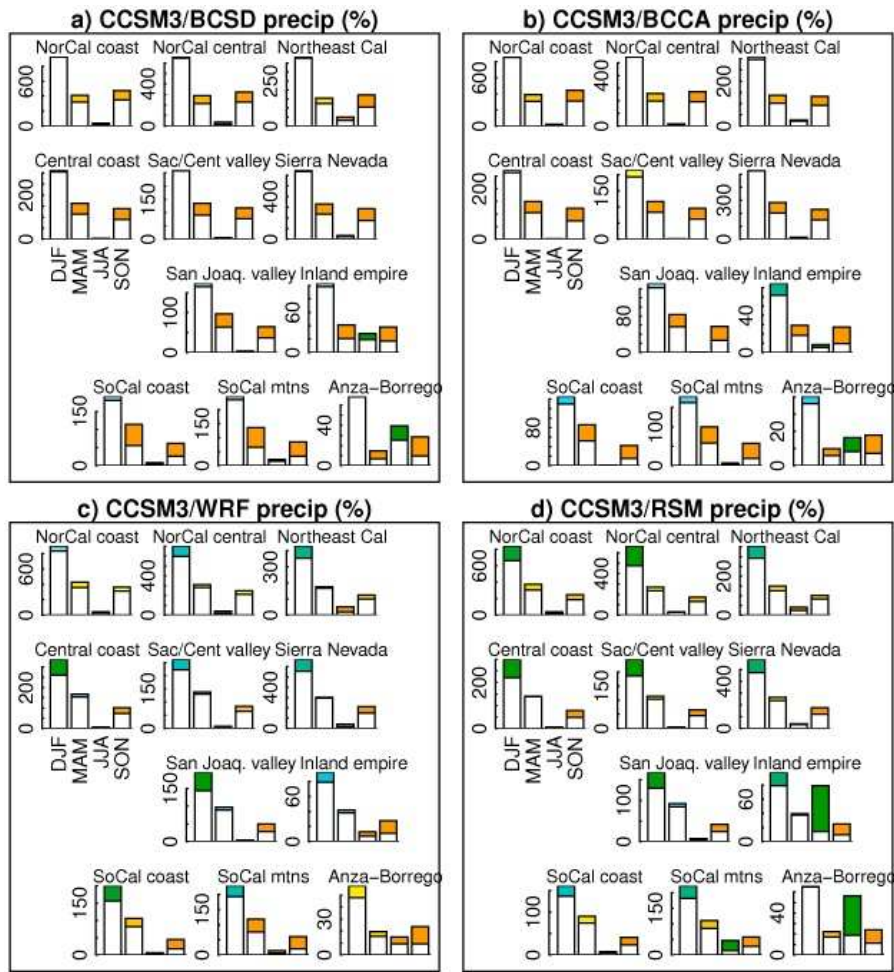
Figure 15. Changes in precipitation for the different downscaling methods applied to the CCSM3 global model. In each panel a-d, the subpanels show the precipitation changes by region, arranged roughly geographically. The bars show each region's seasonal precipitation (mm) in DJF, MAM, JJA, and SON (left to right) in the future and historical periods. The difference between the future and historical precipitation is colored, with the color determined by the percentage change using the same scale as Fig. 10 (yellows/oranges show drying, blue/green show wettening). Note that every set of bars has a different Y axis, in mm.

plot_precip_dels_little_bars_ccsm3_v2.R.jpg
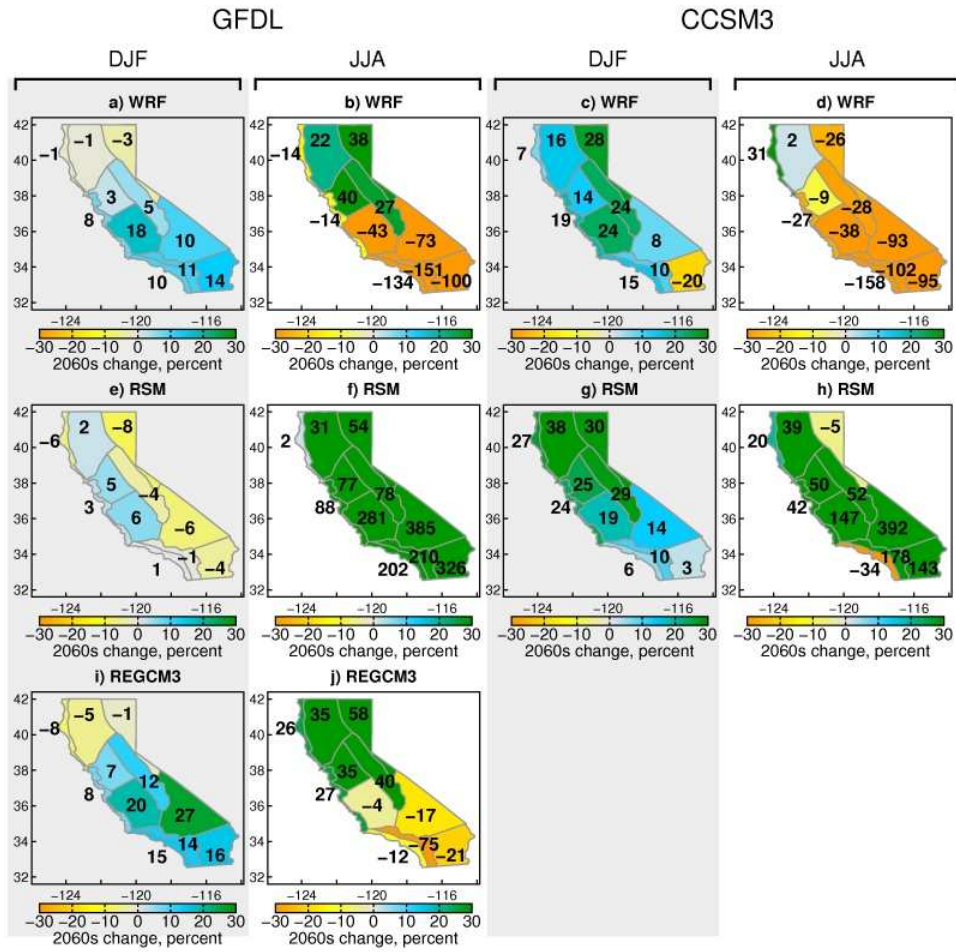
Figure 16. Difference (percentage points) between the change in seasonal precipitation projected by the dynamically downscaled simulations and the change found in the original global model (GFDL 2.1 or CCSM3, as labeled). Only winter (DJF) and summer (JJA) fields are shown.
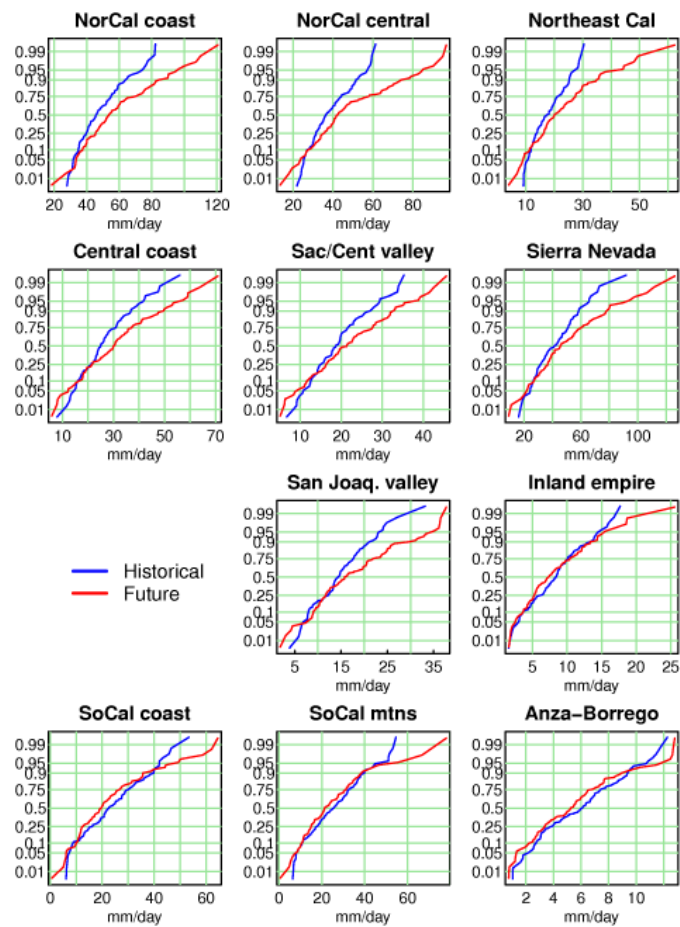
plot_precip_del_of_dels_gfdl_ccsm3.R

Figure 17. Cumulative distribution functions (CDFs) of the maximum 3-day mean precipitation in a calendar year. Regions are plotted roughly geographically. Y axis is probability (0-1) of experiencing the indicated average 3-day precipitation rate (mm/day), or lower.

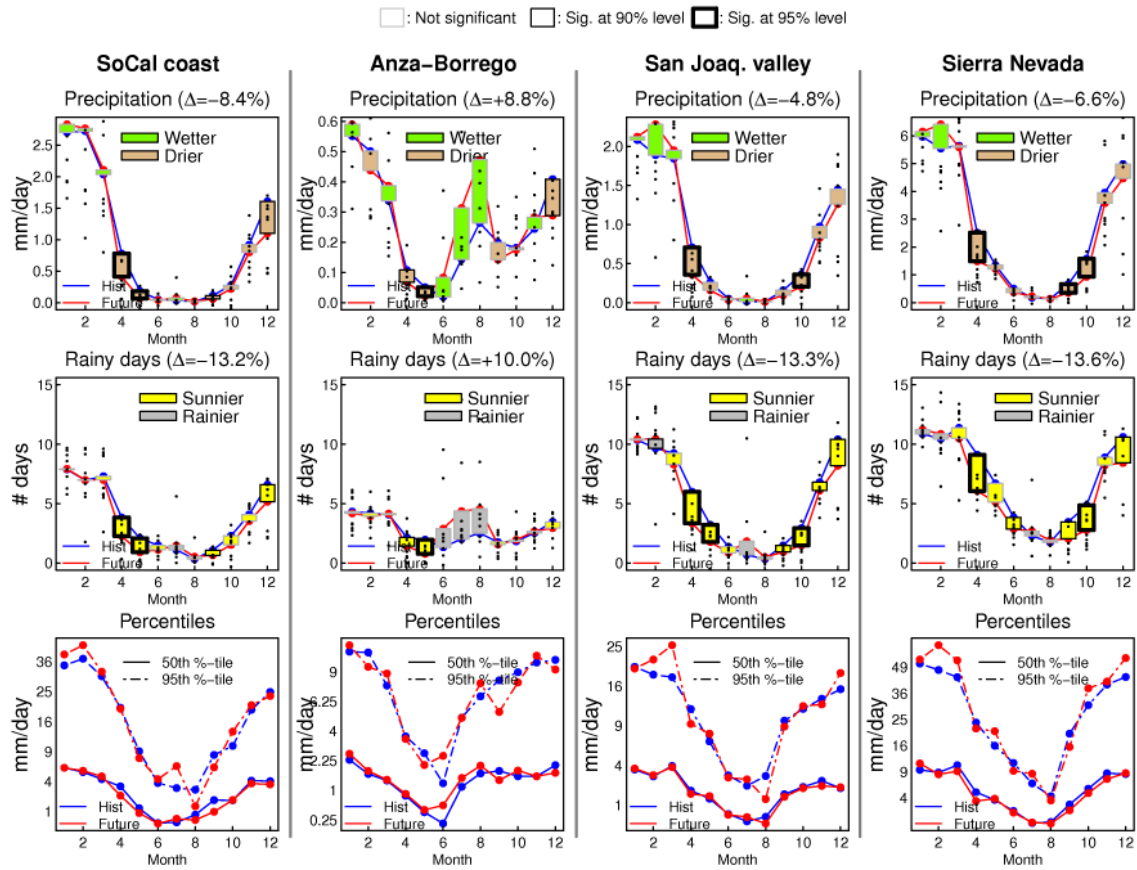/merc02/pierce/data/cec_rcm/forcing/plot_yearly_3daymax.R.ps

Figure 18. Precipitation changes due to storm intensity vs. frequency in 4 regions. Top row: Annual cycle of monthly precipitation (mm/day), for the historical (blue) and future (red) eras. The change in yearly precipitation (%) is in the title. At each month, a box is drawn between the historical and future values; the box is shaded green if the future value is wetter, and brown if it is drier. The box has a heavy outline if the difference is statistically significant at the 95% level, a normal outline if significant at the 90% level, and a light grey outline if not statistically significant. Black dots show individual model values. Middle row: Change in number of days with precipitation ("rainy days"); yellow boxes show a decrease in rainy days, grey boxes show an increase. Bottom row: The 50th (solid line) and 95th (dashed line) percentiles of precipitation, calculated only on days when precipitation occurred, for the historical (blue) and future (red) eras. The Y axis uses a square root transformation to better cover the wide range of values.

plot_change_num_rainy_days_v8.R.01.gif

Figure 19. Apportioning the seasonal precipitation change in each region to changes in storm frequency and intensity. In each set of three bars, the left most (marked "P") shows the change in precipitation during that season (cm). (For comparison, the fractional change in seasonal precipitation is shown at the bottom of each subpanel, in percent.) This bar is colored green for positive (wetter future) changes, and brown for negative (drier future) changes. The middle bar ("Z") shows the change in seasonal precipitation (cm) that arises due to the change in number of zero-precipitation days. Yellow indicates an increase in zero-precipitation days, and grey indicates a decrease. The rightmost bar (marked "I") shows the change in seasonal precipitation (cm) that arises from the change in storm intensity on days with

precipitation. Red shows an increasing intensity, blue shows decreasing intensity. Note that the Y axis varies by region, but for each region is the same across all seasons.
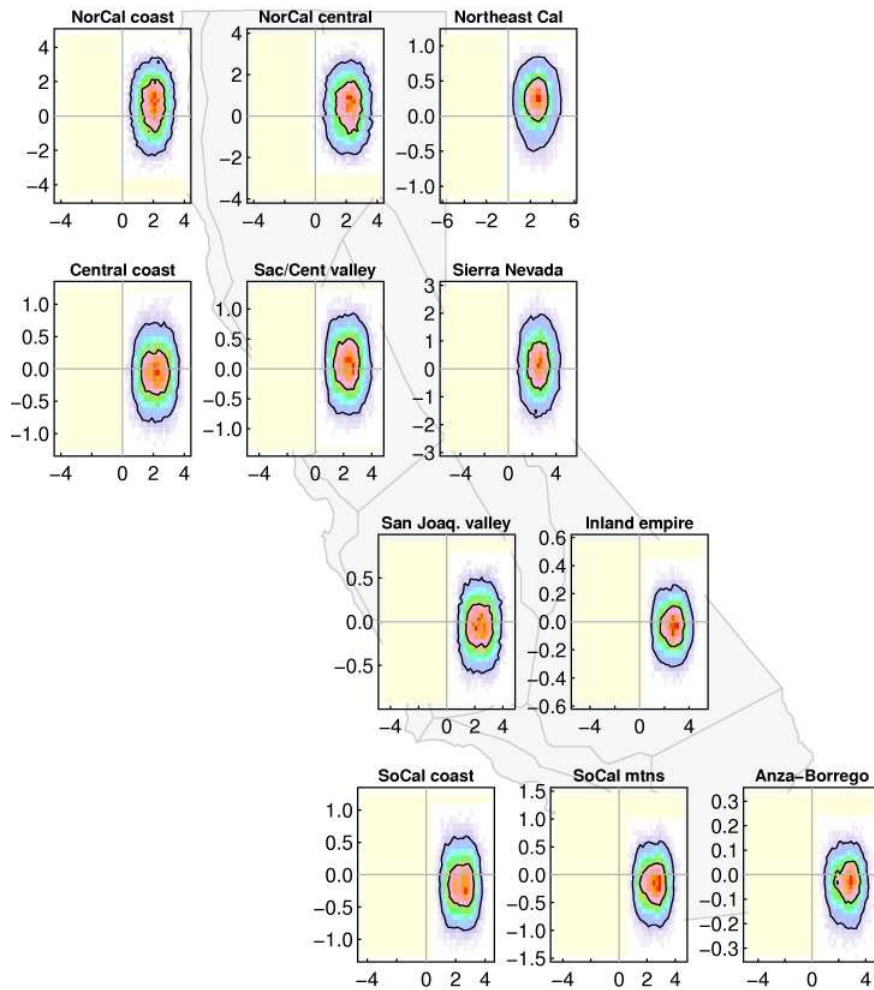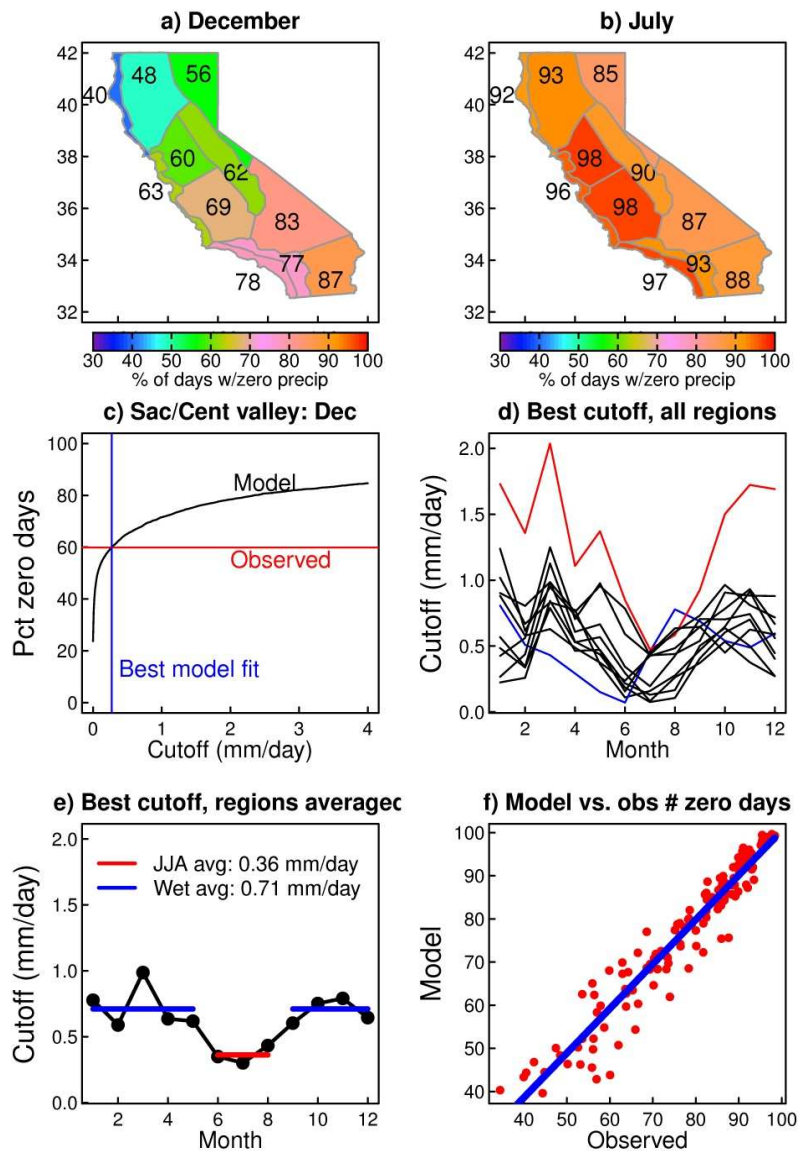
plot_change_freq_intensity_v4.R.gif

Figure 20. Joint distributions of temperature change (degrees C, x axis) and precipitation (mm/day, y axis) in DJF. The outer heavy black line encloses 95% of the data; the inner heavy black line encloses 50%.

mikes_pca_resampling_technique/prob_tp_chagne_2d_v3.R.02.jpg

Figure 21. a) Observed climatological percent of days with zero precipitation, December. b) Same, for

July. c) Black curve shows the percent of zero precipitation days calculated from the model, using data

from December in the Sacramento/Central valley region, as a function of the precipitation cutoff

(mm/day) used. Red line shows observed climatological number of zero precipitation days, and blue line

shows the best-match cutoff that, when applied to the model precipitation, results in the model value

equaling the observed value. d) The best-match cutoff for precipitation (mm/day) for all 11 regions (lines)

and all months. The two outlier regions are the Sierra Nevada (red) and Anza-Borrego (blue). e) The best-match cutoff value averaged across all regions each month. The blue line shows the wet season cutoff value selected for this work (0.71 mm/day), and the red line shows the same for June, July, and August (JJA; 0.36 mm/day). f) The climatological observed number of zero-precipitation days for each month vs. the same value from the model, computed using the wet and JJA values shown in panel e).